CALIBRATION OF ULTRASOUND SCANNERS FOR

SURFACE IMPEDANCE MEASUREMENT

A Thesis Submitted to the

College of Graduate Studies and Research

in Partial Fulfillment of the Requirements

for the Degree of Masters of Science

in the

Department of Mechanical Engineering

University of Saskatchewan

Saskatoon, Saskatchewan

By

Tony Stanley Vollmers

PERMISSION TO USE

In presenting this thesis in partial fulfillment of the requirements for a Postgraduate degree from the University of Saskatchewan, I agree that the Libraries of this University may make it freely available for inspection. I further agree that permission for copying of this thesis in any manner, in whole of in part, for scholarly purposes may be granted by the professor or professors who supervised my thesis work or, in their absence, by the Head of the Department or the Dean of the College in which my thesis work was done. It is understood that any copying or publication or use of this thesis or parts thereof for financial gain shall not be allowed without my written permission. It is also understood that due recognition shall be given to me and to the University of Saskatchewan in any scholarly use which may be made of any material in my thesis.

Requests for permission to copy or to make other use of material in this thesis in whole or part should be addressed to:

Head of the Department of Mechanical Engineering
College of Engineering
57 Campus Drive
University of Saskatchewan
Saskatoon, Saskatchewan
S7N 5A9 Canada

ABSTRACT

The primary objective of this research was to investigate the feasibility of calibrating ultrasound scanners to measure surface impedance from reflection data. The method proposed uses calibration curves from known impedance interfaces. This plot, or calibration curve, may then be used, with interpolation, to relate measured grey level to impedance for the characterization of tissue specimens with unknown properties. This approach can be used independent of different medical ultrasound scanner systems to solve for reproducible tissue impedance values without offline data processing and complicated custom electronics.

Two medical ultrasound machines from different manufacturers were used in the experiment; a 30 MHz and a 7.5 MHz machine. The calibration curves for each machine were produced by imaging the interfaces of a vegetable oil floating over varying salt solutions.

To test the method, porcine liver, kidney, and spleen acoustical impedances were determined by relating measured grey levels to reflection coefficients using calibration curves and then inverting the reflection coefficients to obtain impedance values. The 30 MHz ultrasound machine's calculated tissue impedances for liver, kidney, and spleen were 1.476 ± 0.02, 1.486 ± 0.02, 1.471 ± 0.02 MRayles respectively. The 7.5 MHz machine's tissue impedances were 1.467 ± 0.09, 1.507 ± 0.09, and 1.457 ± 0.09 MRayles respectively for liver, kidney and spleen. The differences between the two machines are 0.61%, 1.41%, and 0.95% for the impedance of liver, kidney, and spleen tissue, respectively. If the grey level is solely used to characterize the tissue, then the differences are 45.9%, 40.3%, and 39.1% for liver, kidney, and spleen between the two machines. The results support the hypothesis that tissue impedance can be determined using calibration curves and be consistent between multiple machines.

To my parents

For inspiring me to explore physics, engineering, and material science

ACKNOWLEDGMENTS

TABLE OF CONTENTS

LIST OF TABLES

LIST OF FIGURES

LIST OF ABBREVIATIONS

DGC – depth gain compensation

GL – grey level

I_{RC} – reflection coefficient intensity

I_{TC} – transmission coefficient intensity

kHz – Kilohertz

MHz – Megahertz

Pixel – Picture element

RC – reflection coefficient

sg. – specific gravity

TGC – time gain compensation

TC – transmission coefficient

US – ultrasound

1. INTRODUCTION

1.0 Overview

Ultrasonography is an extremely useful tool that is primarily used as an *in vivo* method of examining anatomical structures.   Ultrasound (US) is now capable of high resolution real time imaging that is contained in a small, durable, and economical package.   It is testament to the importance of ultrasound that almost 25% of all imaging studies worldwide are ultrasound examinations [1].   With so many machines around the world and with so many manufacturers producing the machines, there is, however, no standard on how the signals received from the internal structures in the body are displayed for the practitioner.   It is, therefore, important to develop a method for analyzing the final image without knowledge of the specific signal processing because signal processing varies widely from machine to machine, and is often inaccessible to the researcher or practitioner.

Assessment of tissue impedance would enhance the use of clinical ultrasonography as a method of non-invasive diagnosis.   For example, changes in tissue impedance may be reflective of cancer or may enable pre-operative prediction of skin plasticity and post-operative repair.   It will be very useful to develop a method of converting the visual output of any ultrasound machine to quantitative impedance values. Ultrasound models are based on the assumption that the signal received from the tissue interface is primarily due to reflection as opposed to scattering.   However, depending on the ultrasound frequency and the nature of the tissue surface, the actual tissue interface may become a scatterer and accepted models cannot be applied.

1.1   Ultrasonography

1.1.1   Principles of Ultrasound

Ultrasound refers to the range of acoustic frequencies which are above the human range of hearing (i.e., frequencies greater than 20 KHz). An ultrasound scanner is used to produce high-frequency pressure pulses that are emitted into soft tissues to create and display a cross-sectional image of the tissue [2], [3], [4], [5]. Medical ultrasound is performed with ultrasound frequencies in the range of 1 – 20 MHz [2], [6]. The high frequency sound waves penetrate the body tissue at a speed of 1450 to 1580 meters per second, depending on the type of tissue [7]. An ultrasound scanner converts energy signals from the console into acoustic signals through piezoelectric crystals.

The transducer is responsible for the transmission and reception of ultrasound waves [2], [3], [4], [5]. The piezoelectric material is a ceramic such as lead zirconate titanium (PZT) that is embedded into an epoxy matrix [1], [2]. The piezoelectric elements can be shaped into rectangular, planar disks, and concave disks depending on the shape of the scanner head and the frequency that is needed. Transducers are made up of a number of layers that facilitate the sending and receiving of the ultrasound pulse. See Figure 1.1 for a simplified diagram of the transducer. Starting at the surface, a typical transducer comprises: 1) a protective layer, 2) a lens, 3) matching layers, 4) an active piezoelectric material (with electrodes and connections), and 5) a backing block [1], [2], [5]. The backing material is applied to the piezoelectric crystal to allow damping to prevent excessive "ringing" of the crystal after excitation. The lens allows the ultrasound energy to be focused upon a fixed area of interest. The matching layers are necessary to allow as much energy into the tissue as possible (i.e., reducing reflections at the transducer-tissue interface).
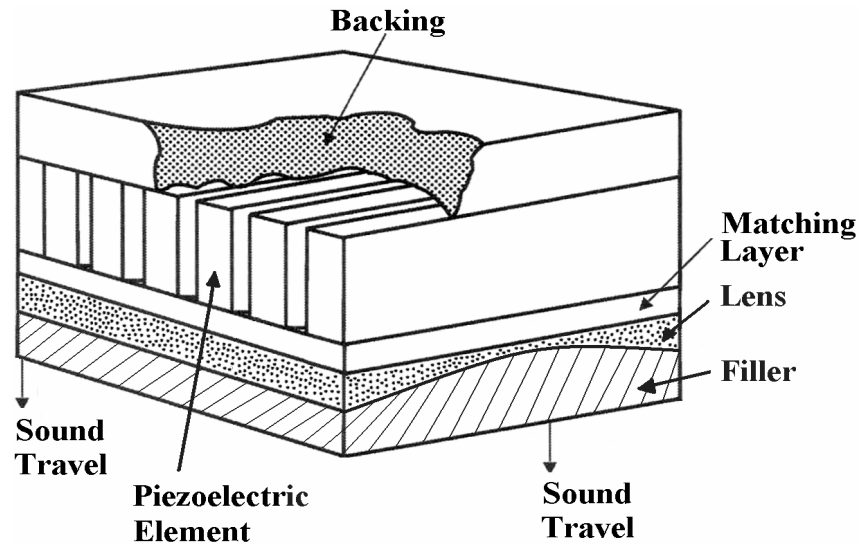
FIGURE 1.1   Internal assembly of a transducer.

1.1.2   Ultrasound Echoes

Once the pulse has entered the tissue a number of factors influence its reflection back to the transducer. Sound waves are reflected only where differences in acoustic impedance occur [2], [8]. Acoustic impedance, Z, is controlled by the tissue density, ρ, and the local sound velocity, c, as shown by:

$$Z = \rho c . \tag{1.1}$$

The metric units of acoustical impedance are Rayles $\left[g \middle/ m^2 \cdot s \right]$. The signal received back from the tissue is influenced by the reflection and scattering of sound waves at organ and tissue interfaces and scattering within heterogeneous tissues [3]. Figure 1.2 depicts the typical causes of attenuation from heterogeneous tissue.
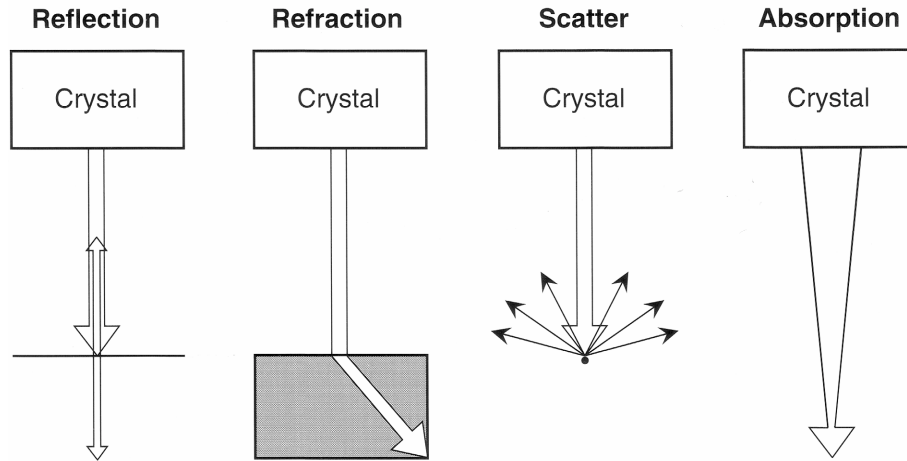
FIGURE 1.2   Attenuation of ultrasound waves passing through different media. Reproduced from [5].

If the ultrasound beam makes perpendicular incidence with an interface of two different impedance materials, then some of the beam will be reflected back towards the transducer while the remainder will be transmitted [2], [3], [5], [8]. The strength of the returning beam will depend on the difference between the impedances of the interface materials. If the incident beam strikes a "smooth" interface at an angle, then the beam will appear to "bend" at the interface. The difference in impedance at the interface determines the angle of refraction. The amount of refraction is predicted by Snell's law

$$\frac{\sin \theta_t}{\sin \theta_i} = \frac{c_2}{c_1} \tag{1.2}$$

where c_1 is the speed of sound on the incident side of the interface, c_2 is the transmitted speed of sound, and θ_t and θ_i are the transmitted and incident beam angles respectively. Snell's law relates the transmitted beam direction to the incident beam direction and the speeds of sound in the two materials forming the interface [2]. An interface that is not perfectly smooth and appears rough with respect to the acoustic wavelength will be a scatterer. If the reflecting object is comparable in size to or smaller than the wavelength, or if a larger object does not have a smooth surface, the incident beam will be scattered [2], [3], [5], [8]. Backscatter is the small portion of the scattered echo that returns to the

transducer. See Figure 1.3 for the difference between interface scattering and scattering within a medium (specular). Modern ultrasound machines rely heavily on scatterers as they indicate tissue parenchyma (echogenicity) and not just the interfaces.

Scattering at an interface   **Scattering within a heterogeneous medium**
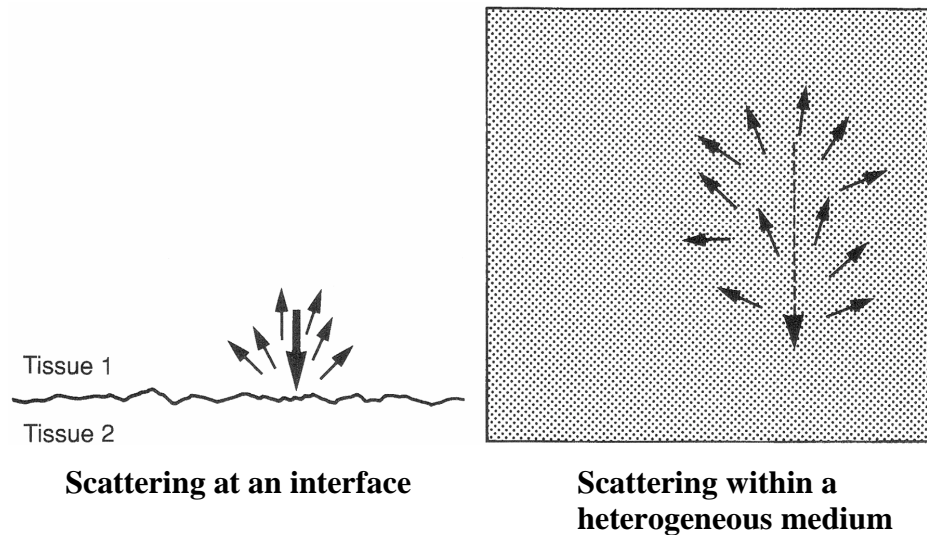
FIGURE 1.3   Ultrasound beam scatterers: A rough and specular example. Reproduced from [3].

Because tissues differ so much internally due to clusters or groups of cells mixed with connective tissue and vasculature, each tissue will vary in echogenicity. As the ultrasound beam travels into the tissue from the transducer, the amplitude and intensity will be reduced. Attenuation encompasses absorption (conversion of sound to heat as the sound propagates) and the refraction and scattering of the sound as it encounters tissue interfaces and heterogeneous tissues [2], [3], [5], [8]. Absorption by a particular tissue is mainly dependent on the intercellular adhesive forces [9].

1.1.3 Ultrasound Imaging

All of the factors described in Section 1.1.2 will influence how the image is formed on the output screen of the ultrasound scanner, but the electronics and the transducer type determines how well they can be represented. Figure 1.4 shows a simplified block diagram highlighting important features of the ultrasound scanning system.
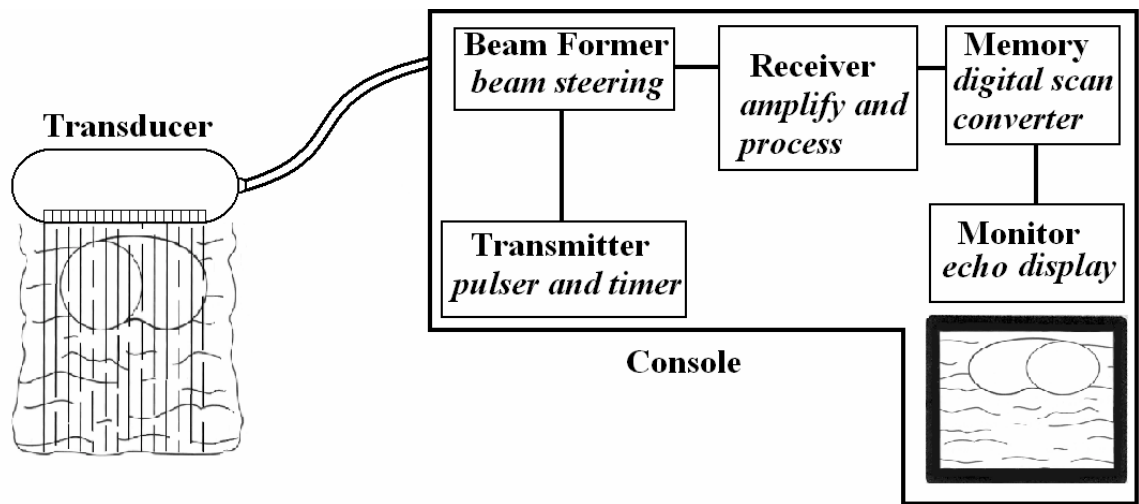
FIGURE 1.4   Simplified components of an ultrasound system. Adapted from [2].

Modern ultrasound imaging is based upon the process of echo-ranging [2], [3], [8]. As each pulse travels into the tissue it undergoes reflection at interfaces. The ultrasound machine will wait for the echo and attribute certain properties to the returned pulse. The properties of the returned pulse can be calculated from two basic equations. The first of these is

$$d = \frac{cT}{2}$$

(1.3)

where d is the distance of an echo causing object from the transducer, T is the time delay, and c is the average speed of sound. The second equation relates the received signal strength to the original signal strength.

$$S(t) = \Gamma(t) \cdot B(t) \cdot A(t) \cdot I(t) \qquad\qquad (1.4)$$

where S(t) is the received signal strength, Γ(t) is the original signal pulse strength, B(t) is a measure of the transducer properties, A(t) is the attenuation of the medium, and I(t) is the strength of the reflected signal. Use of Fourier transforms converts equation (1.4) from the time domain to the frequency domain.

In order to use these descriptive equations, first the ultrasound scanner circuitry must transmit a pulse into the tissue. In pulse emitter mode, the beam former controls the individual piezoelectric elements within the transducer by pulse-delay sequences in order to achieve transmission and reception focus [2], [3], [8]. The pulses from the beam former are controlled by the transmitter clock and control circuitry. Once the pulse has been received back from the tissue, the receiver begins to process the signals for display. The weak analog return signal is first amplified and then attenuation compensation can be applied. Attenuation compensation on ultrasound scanners is called time gain compensation [TGC] and depth gain compensation [DGC] [2], [3], [6], [8]. Compensation can be set by the operator or automatically and is used to equalize the differences in echo amplitude from reflectors at different depths. If on automatic, the receiver will increase the gain as a function of time after each transmitter pulse.

After amplification, the analog signal is converted through an analog to digital converter. The scan converter combines the information from the sensing and control circuitry to produce a scan line. A single scan line is composed of hundreds of *x, y* pixel addresses (position) and *z* pixels (intensities). All of the scan lines are summed together and signal and image processing is applied to give the final output image. The signal processor functions as a filter to eliminate noise and to compress the output signal to the familiar 8 bit or more resolution.

1.1.4   Imaging modes

Most ultrasound books that cover topics in ultrasonography will review the different types of imaging modes [2], [3], [5], [6], [8]. The imaging mode is selected depending on the application. When spatial information is needed A-mode and/or B-mode is selected while if motion and velocity information is needed, then M-mode and/or Doppler is selected. The following section is a brief description of the different modes.

The simplest ultrasound mode is the A-mode output. It is based on the pulse echo technique. The A-mode represents the instantaneous echo signal amplitude versus time after transmission of an acoustical pulse [2]. Each amplitude peak corresponds to a tissue interface of different impedances. The position of the interface can be established by measuring the difference in the peaks. The A-mode output is poor for visualization but the information can be obtained quickly.

B-mode is the natural progression from A-mode where the information is presented as an image. See Figure 1.5 to see how a B-mode image is produced from an A-mode scan. The data from the B-mode is combined to produce a two-dimensional greyscale image. A black to white grey level denotes the intensity. If the pulse does not return from the tissue then it is given a 0 value (black) from the image processor whereas if the pulse returns unattenuated then the grey level value is assigned 255 (white). B-mode is the most commonly used modality in diagnostic practices today.

M-mode is a hybrid of A-mode and B-mode. The M-mode output is comprised of a grey scale output with echo-intensity information overlaid to produce successive images where motion appears as wavy lines on the display. See Figure 1.6 for an example of an M-mode display.
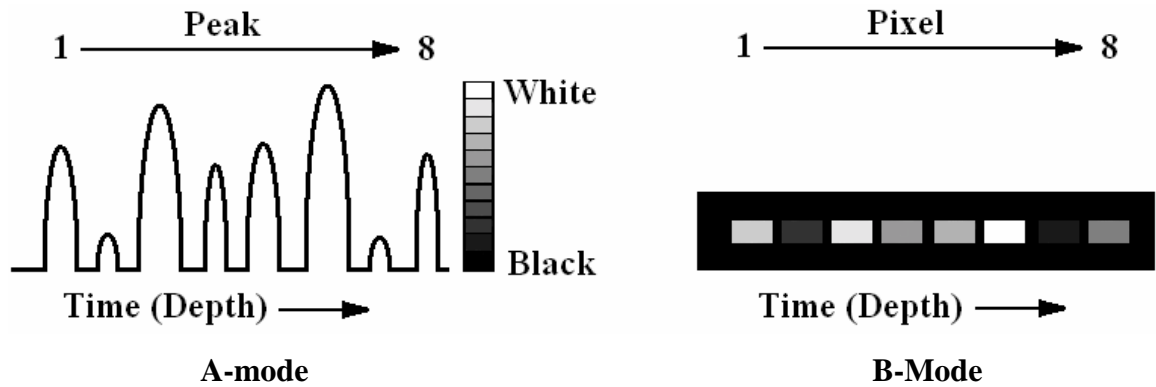
A-mode   **B-Mode**

FIGURE 1.5   Comparison between A-mode and B-mode for the same interfaces and scan line. B-mode is created from the time-amplitude plot of the A-mode.

Quantitative velocity measurements can be obtained from displacements of tissue on the image. Duplex or Doppler mode uses the frequency change of a moving object to assess the velocity of the moving object. By directing the Doppler pulse onto the axis of projection, the colour coded frequency shifted echoes are overlaid on a B-mode image. The flow (away from the transducer or the flow towards the transducer) determines the color of the image.
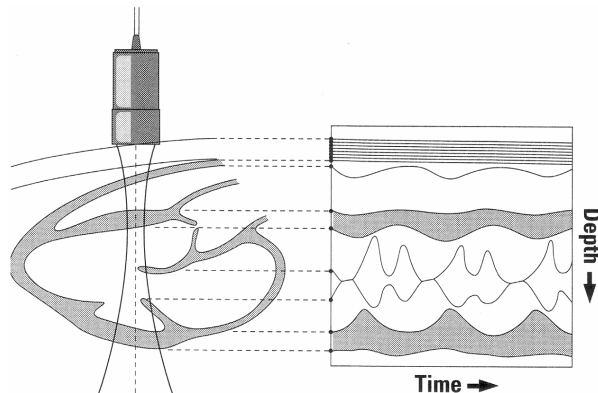
FIGURE 1.6   The M-mode display is produced by taking echo information from one pulse over time. Reproduced from [2].

1.2   Objectives of this thesis

The primary objective of the research was to investigate the feasibility of calibrating ultrasound scanners to measure surface impedance from reflection data. It must be emphasized, from the onset, that the research objective was the design and testing of the calibration method itself. In most medical ultrasound studies, the ultrasonography is used as an imaging tool to test a scientific hypothesis regarding the characterization of tissue and related physiological processes. In contrast, the objective here was to develop and improve the tool itself and the experimental measurement of the tissue impedance was used only to test or verify that the proposed calibration method does indeed constitute an improvement in ultrasound technology.

A secondary objective was to determine if the maximum grey level intensity is just as effective a measure as the conventional mean grey level to measure pixel intensity variation. A comparison between the measures was formulated to satisfy the objective.

1.3   Outline of the Thesis

This thesis is organized into 7 chapters. Chapter 2 reviews the current research into tissue and property assessment through ultrasound. Echotexture research is also reviewed. Chapter 3 describes the fundamental physics and theory behind acoustic ultrasonography. Chapter 4 describes the experimental method of calibrating ultrasound to measure tissue impedances. Results and discussion are covered in Chapter 5. Conclusions are drawn in Chapter 6 while recommendations for future research are in Chapter 7.

2.   LITERATURE REVIEW

2.1   Tissue Assessment through Ultrasound

Ultrasound has progressed past the initial development stage that was solely concerned with producing an adequately high resolution image of tissue. Researchers are now searching within the capabilities of ultrasound to provide more information than the pulse-echo image. The fundamental observation that drives researchers to develop tissue characterization techniques is that many tissue types can be categorized in terms of their acoustical properties and changes in their acoustical properties can be correlated with specific pathological states [10]. Not only is there a connection between acoustical properties and pathological status but modern ultrasound scanners use only a portion of the information available to them, leaving phase and spectral characteristic largely ignored. This section is a brief literature review of some of the tissue characterization techniques that researchers are pursuing.

2.1.1   Image Inspection

Perhaps the oldest and most familiar method of tissue characterization comes from an experienced radiologist being able to relate the texture of an image to the histology [11]. The experienced radiologist, familiar with the settings of the ultrasound machine will be able to differentiate between tissues with different speckle or echogenicity. More specifically, changes in ultrasound-tissue interactions such as attenuation, velocity, and refraction can be detected [12], [13]. Thus, for example, the radiologist can distinguish between the image texture of normal and neoplatic liver tissues [14].

2.1.2   Echotexture Measurement and Analysis

An attempt to quantify image inspection is the echotexture technique. Researchers are using the output of the ultrasound machine to correlate the histological, biochemical, and physiological characteristics of the tissues. The ultrasound output is comprised of a two-dimensional matrix of pixels with each pixel having an x and y coordinate that specifies location and a z coordinate which specifies the pixel intensity [2], [5], [3]. Different tissues at different times will exhibit characteristic appearances through the pixels on the output screen. The characteristic appearance of an examined tissue with an ultrasound image has been referred to as the echotexture of the tissue [5]. Echotexture is characterized by using the average (mean) pixel intensity and the variance of the pixel values within a selected area on a digital image. In order for a computer to analyze analog images, the analog image information must be converted to a digital format. Initially, image echotexture developed from visually comparing grey-scale reference cards to the characterized change in the output image [15], [16], [17], [18], [19]. However, it was very difficult for the user to detect small changes in the pixel values without having a bias. Computer analysis eliminates the subjectivity and is much more sensitive to changes in specific pixels values (color and greyscale) or the distribution of various pixel values (heterogeneity), and can measure very specific areas of an image [20], [21], [22], [23], [24].

Much research is being done using various forms of echotexture. The terminology that is being used includes: texture analysis, speckle analysis, echography, echogenicity, echopattern, and many more. Beekman and Visser have reviewed the capability of echotexture to evaluate the nervous system [25]. The review points to literature that covers normal and abnormal echotexture of peripheral nerves, differentiating muscles from nerves, and possible therapeutic strategies. Statistical analysis of echogenicity was used with high-resolution ultrasound as a method of distinguishing between benign and malignant skin lesions [26]. Echotexture has begun to progress beyond the need for human interaction. Momenan et al. [27], [28] have developed unsupervised analysis from a learning technique that was used to detect tumors and discriminate between neighboring tissues (kidney and liver). The analysis uses 2nd order statistics extracted from speckle in conventional B-scans. Lerski et al.

[29] use texture analysis as possible indicators of histology and pathology for the detection of human liver disease. Increased echogenicity of the kidneys allows for the differentiation of normal and abnormal tissue but does not allow a pathological diagnosis to be performed, and the ultrasound must be used with a biopsy to characterize the pathology [11]. It should be noted that this is just a sampling of the enormous field that is echotexture analysis.

2.1.3 Scattering Characteristics

Because tissues tend to be inhomogeneous and comprised of rough interfaces, there is increasing interest in scattering phenomena and their quantification. However, waves in random media presents one of the most challenging problems to theoreticians [30]. Most studies in scattering characterization center around three principles: frequency dependence of the scatterer, angular reflection of the scatterer, and analysis of the amplitude of the scattered echo.

There are many mathematical models describing how much reflection from scatterers will be returned [31], [32], [33], [34]. Backscatter measurements made on blood, eye, liver, spleen, brain, and heart show the feasibility of differentiating tissues and determining scatterer spacing [35]. It has been shown that for tumors there is a marked disorganization of the cellular structure and those new malignant formations have the same dimension as the wavelengths of ultrasound being used. It is probable that the energy lost by scattering within cancerous tissues exceeds that of the absorption energy [9]. It has also been shown that when the beam strikes the scattering volume the acoustic pressure acting on each point will be different and an averaged or smoothed approach must be used. With this technique Campbell and Waag distinguished between benign and malignant liver scattering and correlated it back to microscopic observations [36]. Heckmatt and Leeman used ultrasonic scattering to define the stage and type of muscular disease in children [37], [38].

Spectral analysis of the backscattered signal must take into account the effects of diffraction which acts like a frequency filter [9]. The spectral analysis technique was developed by Lizzi et al. [39] and King et al. [40]. It can provide theoretical predictions

for scatterer size and concentration [32]. Backscattered spectra can be used to differentiate between tissues (fatty tissue, liver, spleen) [41]. A great deal of research has been directed towards characterizing tissue scattering from the spectra [42], [43], [44], [45], [46], [47]. Angular spectral scattering can only be assumed on tissues that give rise to Bragg scattering. Tissues that are well suited to this analogy are muscular tissue, glandular structures such as the spleen and thyroid, and the liver with its hexagonal lobules [9].

Analysis of the statistical amplitude distribution for diseased and normal tissue was shown to be a useful complementary tissue characterization [48]. The analysis of backscatter spectra provides the backscattering coefficient parameter [33], [49]. The technique characterizes the variations of frequency from a region of interest that is interrogated from different angles. Backscattering spectra were used to characterize hyperplastic spleen and atheromatous aorta specimens [50]. Both tissues exhibited a decrease in the largest peak when diseased. Newer backscatter models are being developed that assume strict boundary conditions in order for the iterative calculations of reflected and transmitted waves at rough interfaces to work [51].

2.1.4 Doppler Signals

The Doppler signal is widely used to study blood flow. This can be used towards tissue characterization by measuring the pulsing of the tissue with time. However a much different detection algorithm must be employed to detect the displacement and frequency of a vibrating tissue [52], [53]. The Doppler technique has been shown to also characterize tumors. In comparison with normal breast arteries and benign lesions, malignant tumors tended to have Doppler signals of higher frequencies [54], [55], [56], [57]. Development of a tumor is associated with the development of new blood vessels. Differentiation of tumor types through duplex Doppler has been clinically proven [58]. Contrast agents, such as encapsulated microbubbles, further enhance blood pools and jets for tissue characterization as well as echogenicity of a malignant tumor [59]. Kruskop et al. [60] used a single A-mode Doppler to measure tissue flow under external

vibration and found tissue elasticity. Charting tissue changes from external stimuli (i.e., drugs) is an emerging field and only preliminary research has been done [61].

2.1.5 Non-linearity of signal propagation

The assumption that ultrasound propagation through media is linear may not be valid [62], [63]. The second order, non-linearity parameter, B/A is used to characterize biological tissue [64]. The variation of velocity is proportional to the B/A parameter by

$$c = c_o + \frac{\left(B/A\right)\Delta P}{2\rho_o c_o} \qquad (2.1)$$

where c is the sound velocity, ΔP is the change in sound pressure, and c_o and ρ_o are the initial sound velocity and density under static pressure [65]. The physical meaning of this expression is connected to the relationship between acoustic pressure and density of a medium. If the acoustic pressure is written as a general series expansion in medium density, then the coefficient of the first order term is A while the coefficient of the second order term is B. The dimensionless parameter is found by solving a Taylor series expansion of adiabatic changes in a medium solved through either a finite element or a thermodynamic method [66] and is related fundamentally to the physical properties of the medium. B/A values have been published in order to create the necessary reference in characterizing tissues. Spleen, liver, breast, kidney, and melanoma have been characterized with the non-linear B/A value [67]. Ichida and Sato have measured B/A values *in vivo* and have produced tomographic images [65].

2.1.6 Motion of Tissue and Elastography

Since echogenicity and the stiffness of tissue may not be correlated, it is expected that imaging tissue stiffness or strain will provide new information that is related to pathological tissue structure. Not everyone agrees that elastic properties of

tissue and echogenicity are not linked and the echographic visibility may be determined by how much collagen resides in the tissue [68]. Certain types of tissues have markedly different elastic properties as compared to surrounding tissues. Elastic tissue methods map the connection between Young's modulus, Poisson's ratio, and viscosity to tissues. It is interesting to note that the primary viscoelastic theory used in elastography is analogous to the relaxation theory in attenuation [69]. Young's modulus has been found for prostate specimens [70] but there is a need to gain more information about this parameter for other tissues such as breast, kidney, liver, and heart for it to be an effective method of tissue characterization.

To study tissue motion, Oestreicher et al. [71], [72] used mechanical vibrations to acquire wave propagation patterns. With the surface wavelength and wave speed they explained that impedance of tissue increases with increased frequency. Using M-mode signals from aortic pulses of the liver, Wilson and Robinson [73] characterized healthy liver tissue. Along the same lines but with A-mode, Dickinson and Hill [74] and Tristam et al. ([75], [76]), evaluated tissue by measuring a correlation parameter between successive A-scans. Using cardiac pulsations of the fetal lung and ultrasound B-mode images, Birnholz and Ferrel [77] postulated that stiff lung tissue transmits cardiac pulsation as a whole rather than local deformations. Eisencher et al. [78] characterized breast and liver tissue with a 1.5 Hz source and M-mode ultrasound. They found that malignant lesions gave rise to an unstructured, non-linear response, while benign lesion responses were sinusoidal.

Sonoelastography images tissue elastic parameters from ultrasound [79]. Stiff tissue will vibrate differently than the surrounding tissue, producing a disturbance in the normal eigenmode patterns [80], [81]. The sonoelastography technique has been extended to liver, breast, and kidneys and *in vitro* prostate cancer [82], [83]. Rubens et al. [84] demonstrated that sonoelastography can be a very sensitive and predictive tool over B-mode images alone. Using A-mode ultrasound and a compression technique (elastography) on tissue sections, Ophir et al. [85] were able to measure the stress and strain fields to produce an elastogram. Ophir's technique is depicted in Figure 2.1. Any *in vivo* tissue that is subjected to a small compression (such as a pulsating artery or respiration) and is accessible ultrasonically can be imaged with elastography. Other

elastic tissue techniques are: forward 2-D analytical compression strain sonoelasticity [86], Inherent strain elastography using a mechanical strain gauge, B-scan images and reconstruction algorithms [87], and tissue motion with speckle tracking [88].

A mechanical method of assessing elastic properties comes from the indentation test [89], [90], [91] where an indenter depresses the tissue and the resulting deformation is recorded. Using an ultrasound transducer mounted with a force transducer, Han et al. [92] were able to estimate linear elastic properties and recover Young's modulus for each layer of a multilayered phantom. To test the quantitative accuracy of ultrasound elasticity values, Chen et al. [93] compared muscle and liver tissue Young's modulus values from a stress-strain Instron experiment to ultrasound derived values. They concluded that the relative error in Young's modulus between the two methods was on the order of 25%.
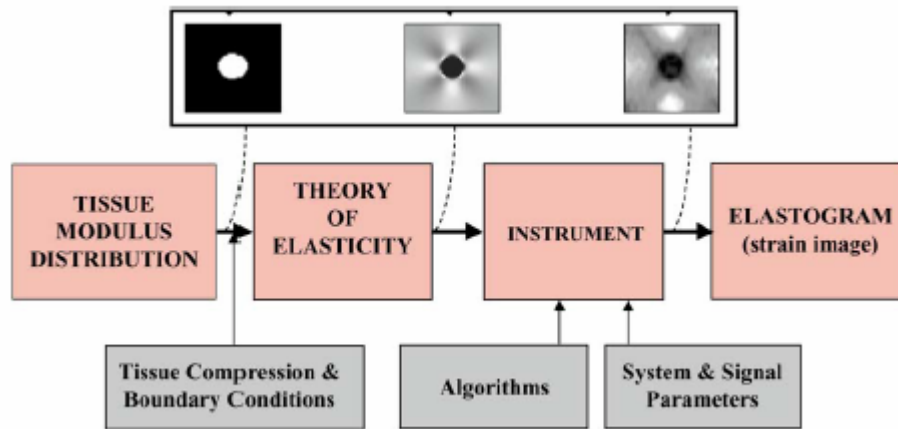
FIGURE 2.1   A block diagram describing the process of creating an elastogram. Reproduced from [94].

2.1.7   Attenuation of Ultrasound

Attenuation can be attributed to absorption, scattering, beam divergence, and wave mode conversion. The two main methods of measuring attenuation are: 1) measuring the difference in peak values between the received waveforms from two depths and 2) measuring the downshift of frequency of the received pulse from two

depths [95]. In order to measure the attenuation within the main methodologies, different techniques can be used such as: transmission, computed tomography, decrement in echo amplitude with increasing range and by the down shift method [11]. Most if not all of the characterization techniques using attenuation rely on the assumption that attenuation has a linear frequency dependence (known only to be an approximation) [10], [95] which is found by using a least-squared error approach from the frequency.

Attenuation measurements depend on these measurement techniques [96] and other factors such as temperature and sample preparation [97]. The methods used to find the attenuation slope can be broadly categorized into time domain and frequency domain methods which are linked by Fourier transformations [95]. The classical theory of attenuation states that absorption occurs when waves within the supporting medium get out of phase with the pressure of the wave [98]. However it has been found experimentally that the classical theory does not hold and that a relaxation process is at work [99], [100], [101]. The majority of the attenuation studies using ultrasound are attempting to characterize liver diseases [102], [103], [104], [105]. Most studies are trying to correlate liver attenuation with histological quantification of fibrosis, necrosis, and fat. Ahuja [106] explains the frequency dependence and large magnitude of attenuation compared to water with the viscoelastic Voigt model [107]. Calderon et al. characterized the differences in attenuation between normal and malignant or benign breast tissue [108]. Miller et al. have shown that frequency dependence of attenuation on canine myocardium can be related to myocardial infarction [109].

Fink et al. proposed using off line Fourier analysis to analyze the A-mode waveform to produce frequency dependent attenuation plots [110]. Ferrari and Jones [111] suggested that the attenuation be based on the assumption that the pulse follows Gaussian propagation and seems to be consistent with other methods. Knowing that the returned A-mode pulse from tissue is a combination of the initial smooth pulse and reflected bumpy pulse some techniques compare the reflected spectrum to the incident pulse [112]. The spectral shift technique has been employed by Dines and Kak [113] to measure the overall attenuation of multilayered tissue from the Gaussian approach developed by Ferrari. More recently attempts have been made to incorporate attenuation

information through pseudo-color maps onto standard B-mode outputs [114]. By using methods developed for X-ray CT reconstruction, tomography can be exploited to reconstruct attenuation coefficients even in the presence of bone and noisy data [115].

2.1.8   Velocity of Ultrasound

Perhaps the oldest tissue characterization technique is from using simple A-mode amplitudes and estimating the resulting tissue sound velocity. First suggested in 1952 by Wild and Reid [116], they were able to distinguish between normal breast tissue and malignant, benign breast lesions. Average tissue sound velocity is usually assumed to be around 1540 m/s with fat at the low end of the range (1460 m/s) and muscle at the high end (1550 – 1660 m/s) [117]. An interesting application of A-mode velocity measurement is to establish whether or not a breast implant has ruptured. A-mode velocities for intact implants were lower (1060 ± 50.1 m/s) than for those that had ruptured (1115 ± 74.3 m/s) [118].   There is much literature in characterizing liver using sound speed [119], [43], [120] as well as sound speed characterizing female breast tissue [121], [122], [117], [123]. Velocity measurements in tissue are important not only to characterize the physiology of tissue but because the resolution and accuracy of conventional ultrasound scanners is so profoundly affected by the distribution of velocities [10]. Unfortunately, velocity measurements *in vivo* are surprisingly difficult to obtain. Using several estimated A-mode amplitudes for 30 different *in vivo* livers, Mountford and Wells [48] characterized the normal tissue using velocity. By means of a simple triangulation, the speed of ultrasound can be estimated in tissues [124]. Goss et al. have shown that sound speed and attenuation decrease with tissue water content and increase with complexity [96]. Robinson et al. has developed a technique where the discrepancy between true sound speed and the assumed sound speed from multiple scanners is calculated from the shift position of an object [125]. If recognizable targets are not visible then the local sound velocity can be calculated from the misrepresentation of tissue boundaries [126]. A useful method of determining sound velocity in superficial organs is the Reference Line Technique by Ohtsuki et al. [127]. Using one transducer along the axis of an organ and a second transducer perpendicular to the organ boundary

at the far end of the organ, the sound speed of the organ can be determined by the axial shift detected by the second transducer. See Figure 2.2 for a depiction of the Ohtsuki technique. A biprism mounted to the aperture of a transducer can determine sound speed by estimating the depth of the target, the angle of the prism, and the distance between the images displayed by a single target [128]. Although the biprism technique is conceptually simple, it suffers from inaccuracy [129]. Haumschild and Greenleaf [130] have investigated a simple method of crossing two beams (two transducers) to estimate the speed of sound. Implementation of the cross-beam technique using beam steering of a multiple array was met with limited success [131] because differing sound speed layers need to be accounted for and inaccuracies arise from the steered beam angle. A beam tracking method first outlined by Ophir [132] uses two perpendicular transducers. One transducer acts as a transmitter and provides a stationary beam while the other acts as a receiver and receives the pulse at different positions perpendicular to the stationary beam. A plot of pulse travel time as a function of distance along the stationary beam is made. A slope of a fitted curve is used to estimate the reciprocal of speed along the path of the transmitted pulse. Subsequent research with the beam tracking method has pushed the precision to 1% for a small region [133].
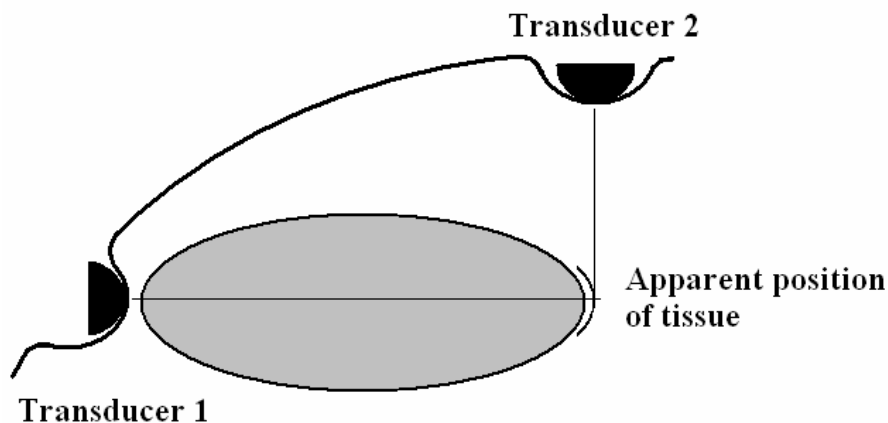
FIGURE 2.2   The sound speed can be estimated by measuring the shift in the apparent position of the tissue with respect to the physical organ boundary.

Characterizing tissues from the velocity has led into computerized reconstructive tomography. Velocity images are created from time-of-flight measurements and incorporated into a reconstruction process [134], [122], [135], [136], [137]. Most time-of-flight techniques have been based on algorithms for X-ray tomography and assume straight line propagation paths. Some techniques have been developed to compensate for the non-uniformity of ultrasound transmission in tomography [138], [139], [140], [141] but are highly susceptible to noise. Dubovikova and Dubovikov [142] suggest using a regularization method to reduce the errors and improve accuracy for noisy reconstructions.

2.1.9   High Frequency Ultrasound and Scanning Acoustic Microscopes

High frequency ultrasound techniques generally use ultrasound methods already developed for tissue characterization but at higher resolutions. High frequency acoustic microscopes operate in the frequency range of 10 MHz to 5 GHz. The penetration depth is low however the resolution is comparable to that of optical microscopes [143]. Hozumi et al. [144] characterized cardiac tissue using sound speed and a 50 to 150 MHz ultrasonic microscope. The technique used reflections from the front and rear sides of the sliced tissue and time-frequency analysis. Santosh et al. [145], [146] analyzed reflection from a 10 MHz pulse from the human eye and plaque deposits on the wall of an artery.

Many medical papers discuss the ability of emergent high frequency ultrasound systems to discriminate between malignant and benign breast tumors [147] and dermatological cancers [148]. High frequency ultrasound systems can be over 90% specific in determining breast cancer. High frequency ultrasound in the 7.5 to 13 MHz range has sufficient resolution to clearly detail the three layers (epidermis, dermis, and subcutaneous) of normal skin [149] and is able to measure the thickness of cutaneous melanoma, an important prognostic factor. Using inverse scattering theory they were able to recover profiles of acoustic impedance for cutaneous melanoma with features of 50 μm being resolved. Ultrasound biomicroscopy can show the frequency-dependance

of attenuation within skin, arteries, heart, liver, muscle, blood, cornea and other tissues with high resolution [150].

Scanning acoustic microscopes (SAM) operate differently than typical ultrasound scanners in that they excite the surface of the material to produce acoustic waves. By detecting the acoustic waves, the acoustic properties of materials at a high resolution are achieved. Imaging of biological samples at the angstrom level is possible as well as previously difficult tissues to image with ultrasound (such as lung) [143]. Amplitude and phase characterization has been done on metal composites with SAM but has yet to be performed with biological tissue [151], [152].

2.1.10 Acoustic Impedance

If the scattering is weak and scattering from fluctuations in absorption can be neglected, then the only tissue acoustical property contributing to the backscattered signal is the characteristic impedance [10]. This observation is supported in both simplistic one-dimensional reflection models (reflection coefficient) and by complicated, three-dimensional scattering models from inhomogeneous media [153]. Impedance can be estimated by correcting for overlying tissue attenuation and geometry [154]. Impedance characterization has found a niche in characterizing tumor blood vessels which are deficient in muscular elements and are of low impedance [11]. Calcification of heart tissue can be detected because it involves changes in impedance [97]. Using a simple model and a temperature controlled water bag, Ogura et al. [155] measured the acoustic impedance of abdomen and breast skin. The severity of atherosclerotic arteries from their acoustic profiles was investigated by Tobocman et al. [156]. The acoustic profiles of the arteries were obtained using an attenuation compensation technique and backscatter spectral analysis.

Jones and Cole-Beuglet [157] found that intra-ocular and orbital lesions can be detected and displayed through an impedogram (profiles of acoustical impedance). Impedography is a general method of reconstructing the impedance profile from the impulse response of the investigated medium. Initially a one-dimensional technique

[158], it has evolved into a three-dimensional model assuming that the wave-fronts remain planar [159]. Pederson et al. used the impedography technique (a non-recursive method) and compared it to the geological reconstruction algorithm of Goupillaud (a recursive technique) [160]. The research showed that when noise was present the Goupillaud method is far better for reconstruction of the acoustic impedance profile of a layered medium. Acoustic impedance profiling of a layered medium from reflected pulses and *a priori* knowledge of the transducer and attenuation of the medium was performed on a 3-layer phantom by Pederson and Lifshitz [161], [162]. A reflection model was suggested and the inversion is performed with a Wiener filter to compensate for noise inherent in the signal. This technique has been extended to reconstructions of media with resolutions as fine as 48 μm [163].

2.1.11 Non-biological Material Property Measurement Through Ultrasound

To complete this literature review, it should be acknowledged that many ultrasound techniques have been applied to the material science arena. In a manufacturing process it might be useful to determine a particular property of a material which is imbedded in another. Most material property techniques are simpler methods than tissue characterization techniques and only deal with homogeneous materials being perpendicular to the transducer.

Detection of the thickness of air gaps inside composite materials is accomplished by detecting the increase in the measured attenuation [164]. Bramanti [165] suggested a technique where impedance, attenuation and acoustic velocity of a material in a water bath can be determined. The method is based on the reflection coefficient and frequency. A curvature compensated boundary reflection assessment method for determining acoustic impedance inside oil pipelines is described by Gunarathne and Konstantinos [166]. The method uses sequential A-mode scans inside the petroleum pipe and a curvature compensated algorithm to automatically classify impedance profiles. In order to identify recyclable polymeric materials and components, Hull et al.

[167] used an ultrasound attenuation and time of flight method to separate the recyclables from waste streams.

2.2   Concluding Comments

There is a need for a quantitative parameter that is reproducible from one recording to another, from one patient to another [9]. Conventional B-mode images are not quantitative images for two reasons. Firstly, image densities depend on system settings and the choice of transducer. Secondly, even if settings and transducers could be allowed for, the resultant image would be a reflectivity map of the tissue which is a complicated function of both tissue interaction parameters as well as tissue morphology [37]. All of the foregoing techniques and methods require specialized machines or laboratory conditions.

The purpose of this thesis is to provide a simple, effective means of characterizing tissue with any conventional ultrasound machine. Including a table of acoustical properties of common materials and tissues concludes this section. The table shows the comparisons between tissue characterization techniques such as: velocity, impedance, attenuation and frequency of attenuation on tissue and 2 reference substances.   The table was copied from Jones and Leeman [10].

TABLE 2.1

Material	Propagation velocity [m/s]	Characteristic impedance $[10^6 \cdot kg/m^2 s]$	Attenuation at 1 MHz [dB/cm]	Frequency dependence of attenuation
Water (20°C)	1480	1.48	0.0022	f^2
Aluminum (bulk)	6300	17	0.018	F
Air (std.)	343	0.000415	12	f^2
Blood	1570	1.61	0.18	$f^{1.3}$
Brain	1541	1.58	0.85	$\sim f$
Fat	1450	1.38	0.63	$\sim f$
Human soft tissue (mean)	1540	1.63	0.81	$\sim f$
Muscle	1585	1.70	$1.3 - 3.3$	$\sim f$
Skull bone	4080	7.80	13	F^2
Lung	650	0.26	41	f^{-1}

Acoustical properties of several common materials [10]

3.   THEORY OF MEASUREMENT

3.1   Ultrasound Wave Propagation

Ultrasound propagates both as transverse and longitudinal pressure waves. In tissues, sound waves only travel as longitudinal waves [2], [3]. Consider an element of length dx within an elastic medium which is being acted upon by the passage of a sound wave, as shown by Figure 3.1.
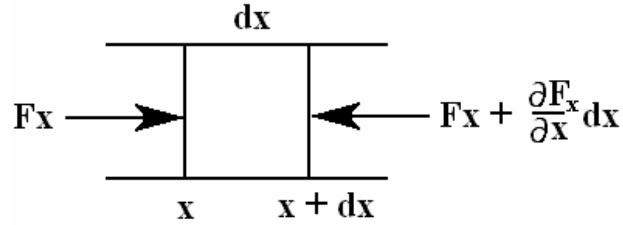
FIGURE 3.1   Forces on an element during the passage of a sound wave.

As the wave propagates through the medium, it must obey Newton's second law,

$$\sum F_x = ma \tag{3.1}$$

where ΣF_x is the instantaneous net force on the element, m is the mass of the element, and a is the instantaneous acceleration of the element. Due to pressure variations within the medium, if one face experiences a force, the force on the opposite face will be, in general, $F_x + (\partial F_x / \partial x)dx$. Referring to Figure 3.1 the difference in the forces is

$$dF_x = \left(F_x + \frac{\partial F_x}{\partial x} dx \right) - F_x = \frac{\partial F_x}{\partial x} dx \, . \tag{3.2}$$

Considering the same element, the displacements of the element are shown by Figure 3.2. During the passage of the sound wave the left face of the element will have moved a distance ξ and the right a distance $\xi + d\xi$.
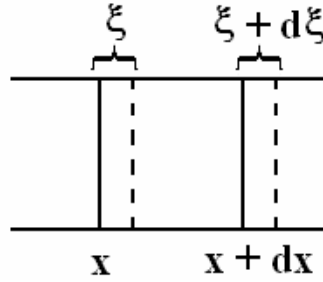
FIGURE 3.2   Displacements of the element during the passage of a sound wave. Reproduced from [168].

The change of length of the element is then

$$d\ell = (\xi + d\xi) - \xi = d\xi = \frac{\partial \xi}{\partial x} dx \tag{3.3}$$

where $d\ell$ is the change in the length of the element. The resulting axial strain on the element is then

$$\varepsilon = \frac{d\ell}{dx} = \frac{\partial \xi}{\partial x} \, . \tag{3.4}$$

To relate the strain and the axial force for a linear elastic medium, Hooke's law is used

$$E = \frac{\sigma}{\varepsilon} \tag{3.5}$$

where E is the modulus of elasticity and σ is the axial stress. The stress for this axial case is given by

$$\sigma = \frac{F}{A} \qquad (3.6)$$

where A is the area of the face on which the force is applied. Combining equation (3.5) with equations (3.4) and (3.6) gives

$$E = \frac{F/A}{\partial \xi / \partial x} . \qquad (3.7)$$

Rearranging equation (3.7) gives

$$F_x = AE \frac{\partial \xi}{\partial x} , \qquad (3.8)$$

which is the force on the left face of the element. Taking the partial derivative of equation (3.8) and substituting into equation (3.2) gives the expression for the net force on the element considering homogeneous elastic properties,

$$dF_x = AE \frac{\partial^2 \xi}{\partial x^2} dx . \qquad (3.9)$$

Knowing that mass and acceleration of the element can be written as

$$m = \rho (A \, dx) \qquad (3.10)$$

and

$$a = \frac{\partial^2 \xi}{\partial t^2} \qquad (3.11)$$

where ρ is the density of the medium and t is the instantaneous time, equation (3.1) becomes

$$dF_x = \rho A \frac{\partial^2 \xi}{dt^2} dx.$$
(3.12)

Equating equation (3.9) with (3.12) yields the sound wave transmission equation (or simply the wave equation)

$$\frac{\partial^2 \xi}{\partial t^2} = C_\ell^2 \frac{\partial^2 \xi}{\partial x^2}$$
(3.13)

where

$$C_\ell = \sqrt{\frac{E}{\rho}}.$$
(3.14)

For plane longitudinal waves, equation (3.13) is the one-dimensional form of the wave equation. Two-dimensional and three-dimensional wave propagation is formed from the same equations [169] but is not covered in this thesis. The constant C_ℓ is the propagation speed of a disturbance within the medium. From equation (3.14) it is obvious that the wave propagation speed is only a function of the properties of the medium and not on the frequency or wavelength of the disturbance.

Ultrasound excitation within media is known as simple harmonic motion. If the medium is excited by a pulse with angular frequency of ω radians per second, the resulting particle within the medium will displace

$$\xi = Ae^{j(\omega t - kx)}$$
(3.15)

where ω is the angular frequency, k is the wave number and the maximum displacement of the particle is given by A, the amplitude. Equation (3.15) is complex because the angle of vibration may be out of phase with the direction of propagation. As successive

waves propagate into the medium, they are separated by a distance of one wavelength, λ given by

$$\lambda = C_1 / f = (2\pi C_1) / \omega \tag{3.16}$$

where f is the harmonic excitation frequency in cycles per second (Hertz). The wave number, k, is the number of complete waves in 2π meters (in SI). It can be related back to the speed of wave propagation and angular frequency by

$$k = \omega / C_\ell \ . \tag{3.17}$$

3.2 Acoustic Impedance

A wave front reflection at interfaces between two media of different acoustic impedance is a fundamental property of ultrasound. An impedance difference within and between tissue governs how intense the return echo on the output screen appears. Impedance is given by

$$z = p / u \tag{3.18}$$

where p is the instantaneous pressure of the medium at a point and u is the instantaneous particle velocity ($\dot{\xi}$) at the same point. Equation (3.18) is the characteristic impedance of the medium and it is analogous to electrical impedance ($R = V/I$). It is equal to the mechanical impedance per unit area of the cross section of the medium. The pressure in an elastic medium can be written as a stress,

$$p = E \frac{\partial \xi}{\partial x} \tag{3.19}$$

where E is the Young's modulus and $\partial \xi / \partial x$ is the strain. Substituting equations (3.15) and (3.19) into (3.18) expresses impedance as a frequency dependent term yielding

$$z = -E(k/\omega). \tag{3.20}$$

Furthermore, using equations (3.17) and (3.14) converts the impedance equation into the more familiar expression of

$$z = -\rho C_\ell. \tag{3.21}$$

A final simplification is to use only the absolute magnitude of impedance (because the present discussion is not interested in determining the reactive component, only the resistive) so

$$z = \rho C_\ell. \tag{3.22}$$

3.3   Transmission and Reflection at an Interface

If a sound wave meets the interface of two different media with two different impedances, the sound wave will be partially reflected and partially transmitted. See Figure 3.3 for the behaviour of the wave at the boundary of two different impedances. The particle velocity of the incident beam can be found by taking the partial derivative of equation (3.15) with respect to t:

$$u_i = U_i e^{j(\omega t - kx)} \tag{3.23}$$

where U_i is the velocity amplitude of the incident wave. Similarly, the equations for the reflected and transmitted waves are

$$u_r = U_r e^{j(\omega t + kx)} \tag{3.24}$$

and

$$u_t = U_t e^{j(\omega't - k'x)} \tag{3.25}$$

where the primed terms indicate the wave traveling in medium 2. The positive and negative signs for kx indicate the direction of travel of the wave from the interface.

Incident Reflected
[i]   [r]

Medium 1
E
C
ρ

x = 0

Medium 2
E´
C´
ρ´

Transmitted
[t]
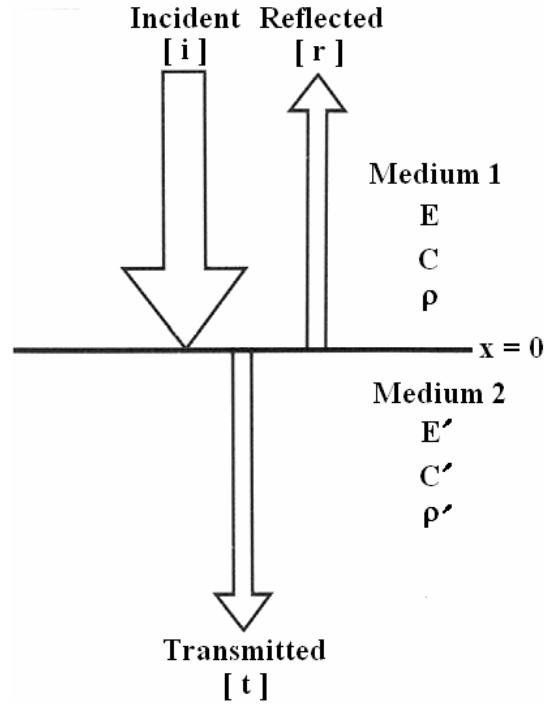
FIGURE 3.3   Reflection and transmission at a boundary perpendicular to the wave propagation.

Under the condition that the media are continuous, which holds at the boundary, the resultant particle velocity (or particle displacement) of the incident and reflected waves must equal the particle velocity (displacement) of the transmitted wave, otherwise a discontinuity would appear at the boundary [169]. Therefore, if continuity of the particle's velocity, stress, and frequency is assumed at the boundary between the two media, then

$$u_i + u_r = u_t. \tag{3.26}$$

Substituting equations (3.23) – (3.25) into (3.26) yields

$$U_i e^{j(\omega t - kx)} + U_r e^{j(\omega t + kx)} = U_t e^{j(\omega' t - k'x)}.$$ (3.27)

The assumption of frequency continuity at the interface requires that $\omega = \omega'$ at $x = 0$. Therefore, at the interface the exponential terms cancel and disappear leaving

$$U_i + U_r = U_t.$$ (3.28)

The frequency dependent pressures at the interface can be written as

$$p_i = P_i e^{j(\omega t - kx)},$$ (3.29)

$$p_r = P_r e^{j(\omega t + kx)}, \text{ and}$$ (3.30)

$$p_t = P_t e^{j(\omega' t - k'x)}.$$ (3.31)

Similarly, the pressure (stress) across the boundary is written as

$$p_i + p_r = p_t$$ (3.32)

and solving for pressure continuity across the boundary from equations (3.29) – (3.31) and (3.32) yields

$$P_i + P_r = P_t.$$ (3.33)

The materials' specific impedances are given by equation (3.18) such that

$$z_1 = P_i / U_i,$$ (3.34)

$$z_1 = -P_r/U_r \text{, and} \tag{3.35}$$

$$z_2 = P_t/U_t . \tag{3.36}$$

Note that the reflection impedance in equation (3.35) is negative with respect to the transmitted (3.36) and incident (3.34) impedance equations. The negative sign arises from the reflected wave propagating in a direction opposite to the incident and transmitted wave.

Combining equations (3.36) with (3.33) and (3.28) yields

$$z_2 = \frac{P_i + P_r}{U_i + U_r} . \tag{3.37}$$

Further manipulations of (3.37) using equations (3.34) and (3.35) results in the reflection coefficient [RC]

$$RC = \frac{P_r}{P_i} = \frac{z_2 - z_1}{z_2 + z_1} \tag{3.38}$$

and the transmission coefficient [TC]

$$TC = \frac{P_t}{P_i} = \frac{2z_2}{z_2 + z_1} . \tag{3.39}$$

The pressure reflection and transmission coefficients, which determine the amplitude of the pressure in the reflected and transmitted waves depend heavily on which medium the wave enters. If the mediums are of the same impedance ($z_1 = z_2$) then no reflection will occur. If the wave starts in a medium of high impedance then propagates across a boundary into a medium of low impedance ($z_1 \gg z_2$), the reflection coefficient will be -1 (the negative indicates a change of phase for the reflected wave).

If the wave starts in a medium of low impedance then propagates into a medium with high impedance ($z_1 \ll z_2$), the reflection coefficient will be 1 and will have no phase change. However for the transmitted wave, a low to high impedance ($z_1 \ll z_2$) boundary will represent an amplification of the wave. The pressure ratios at boundaries of differing impedances are summarized in Table 3.1.

TABLE 3.1

Reflection and transmission coefficients at boundaries			
	$z_1 = z_2$	$z_1 \gg z_2$	$z_1 \ll z_2$
$RC = \dfrac{P_r}{P_i}$	0	-1	1
$TC = \dfrac{P_t}{P_i}$	1	0	2

3.4   Power Intensities

Pixel intensity as represented on the output of the ultrasound screen is a combination of power intensity per unit area of the wave front and the scanner electronics. The power intensity is defined as power = stress multiplied by the displacement velocity. The derivation of the power expressions for the incident, transmitted, and reflected waves is similar to that of the pressure ratios [168] and is

$$Pwr_i = \frac{1}{2}\frac{EA_i^2\omega^2}{C_1}, \tag{3.40}$$

$$Pwr_t = \frac{1}{2}\rho'C_1'A_t^2\omega^2, \text{ and} \tag{3.41}$$

$$\mathrm{Pwr}_r = \frac{1}{2}\rho C_1 A_r^2 \omega^2.$$

(3.42)

Using the same assumption of continuity across the boundary and through algebraic manipulation using equations (3.40) – (3.42) with equation (3.22) yields the reflection coefficient intensity [I_{RC}] and transmission coefficient intensity [I_{TC}]

$$I_{RC} = \frac{\mathrm{Pwr}_r}{\mathrm{Pwr}_i} = \left[\frac{1 - z_2/z_1}{1 + z_2/z_1}\right]^2$$

(3.43)

and

$$I_{TC} = \frac{\mathrm{Pwr}_t}{\mathrm{Pwr}_i} = \frac{4[z_2/z_1]}{[1 + z_2/z_1]^2}.$$

(3.44)

Note that Equation (3.43) gives simply the square of the quantity on the right hand side of Equation (3.38). This is as expected, since the energy of the wave is known to be proportional to the square of its amplitude. Equation (3.43) is used throughout the thesis to relate the impedances of the interfaces in the experiment (Section 4.1). This is a simplified physical model of the ultrasound return intensity and is valid only because of the planar or almost planar interfaces involved in both surface impedance measurements and the calibration method itself. In the future, for non-planar surfaces and structures below the surface, a more complicated model will be needed that relates the reflection coefficient intensity with attenuation and scattering phenomena. There is an immense amount of literature available on more sophisticated models (see Chapter 2) of ultrasound physics that can be used to this end.

4. EXPERIMENTAL METHOD

4.1 Calibration Experiment: Oil-Salt Solution Interfaces

In order to characterize tissue with any conventional ultrasound scanner, a calibration curve was necessary to relate grey level to acoustical impedance. The calibration experiment produced images of two liquid layers of different impedance and produced plots of grey level intensity versus reflection coefficient intensities (Equation 3.43). Each set of liquid layers produces a single interface consisting of one layer of oil floating over a layer of salt solution. The same oil, of known impedance, was used for each interface. The impedance of each salt solution was set by controlling the concentration of salt. To get a large enough sampling of data for the curves, the salt solutions were varied from 0% to 20% salt concentration in 2% increments. Each oil layer and salt solution concentration was used to produce one data point on the calibration plot.

The mass of salt required for the preparation of each solution was determined by referring to the CRC handbook of Chemistry and Physics [170]. This manual gives the precise mass of ACS grade salt to be mixed with distilled water to produce a particular anhydrous solute weight per cent (g solute/ 100 g solution). Using a Canlab Sartorius 1000 g analog mass scale (VWRCanlab, Edmonton, Canada) and a 500 mL beaker, the required mass of salt was obtained for a 3 L solution. A 5% mass addition was used to compensate for the volume displaced by the salt in the solution. Using a 3.5 L graduated beaker to measure 3 L of distilled water, the salt was added and mixed using a mixing bar on a hot plate. The solution was mixed until it was visually apparent that there was no longer any solute. Once the solutions were properly mixed, they were poured into 4 L plastic jugs and left to sit overnight. An ERTCO (Ever Ready Thermometer Co, Dubuque, USA) precision hydrometer (specific gravity from 1.000 to 1.220) was used to determine the precise specific gravity of the solution. Following the ASTM test standard [171] the specific gravity was recorded as was the solution temperature in

degrees Celsius. The specific gravity reading was then calibrated for temperature with the supplied ERTCO Correction for Specific Gravity Hydrometer data sheet (See Appendix A for the reproduced data correction sheet). Because the temperatures measured in the solution did not correspond exactly to the values on the data sheet, a linear interpolation was used to solve for the correction factor at each measured temperature. Since the correction factor depends on the nominal specific gravity as well as the temperature, the correction factor needed at the measured specific gravity was found by using another linear interpolation. Finally the correction factor was applied to the nominal specific gravity to find the calibrated specific gravity. The calibrated specific gravity value was compared back to the CRC handbook to find what the actual anhydrous solute weight per cent was present in the solution. Impedance values for 0%, 10%, 15%, and 20% salt solutions were found in published material [172] and a second-order quadratic (4.1) was used to relate the percent salt solution to the impedance using Microsoft Excel 2003 (Microsoft Corporation, Redmond, USA).

$$z = 8.4997 \times \left(\frac{\% \, \text{Salt Solution}}{100} \right)^2 + 0.0467 \times \left(\frac{\% \, \text{Salt Solution}}{100} \right) + 1.49 \tag{4.1}$$

where z is the impedance of the solution. The fitted equation has a coefficient of determination of 0.9985 where 1 is a perfect fit. The coefficient of determination is defined by

$$R^2 = 1 - \frac{\text{SSE}}{\text{SST}} \tag{4.2}$$

where $\text{SSE} = \sum \left(Y_j - \hat{Y}_j \right)^2$, $\text{SST} = \left(\sum Y_j^2 \right) - \frac{\left(\sum Y_j \right)^2}{n}$, Y_j are the best least-squares quadratic fitted data, and $\hat{Y}_j$ are the data points. Equation 4.1 was necessary because more salt solution concentrations (0% to 20% in 2% increments) were used than the published data provided.

Two ultrasound machines were used for the research: a VisualSonics Vevo 660 High Resolution Imaging System equipped with a 30 MHz probe (VisualSonics Inc., Toronto, Canada) and a 7.5 MHz Aloka SSD-900 linear array (Aloka Co. Ltd., Tokyo, Japan). The two product specifications are given in Table 4.1. In order for the images from the Aloka SSD-900 to be saved, a Pentium II computer with a FlashBus Spectrim Lite (Integral Technologies, Indianapolis, USA) video capture card was used. FBG 32 video capture software (Integral Technologies, Indianapolis, USA) with 640 X 480 max. resolution was used on the computer to capture the interface images.   The settings for the Vevo 660 and the Aloka SSD-900 were standardized throughout the observation period at predetermined values (but not between the two machines). The group of 8 STC slider resistors which adjust gain at each display depth were kept at the zero position and the ABC button, which automatically adjusts the B mode image sensitivity, was turned off. The 7.5 MHz scanner of the Aloka SSD-900 was set to high resolution (R mode) image select and the line density, which controls the scanning line density of a black and white image, was set to high (H mode). The settings of the Aloka SSD-900 are given in Table 4.2 and the associated FBG 32 image-grab software settings are given in Table 4.3. The Vevo 660 settings are in Table 4.4

TABLE 4.1

Product specifications of the ultrasound transducers		
Manufacturer:	Aloka	VisualSonics
Operating Frequency:	7.5 MHz	30 MHz
Probe:	UST-5821-7.5	VS-RMV30A
Focal Length:	64 mm	12.5 mm

The interfaces for the Vevo 660 were created within 900 mL graduated glass beakers with approximately 400 mL salt solution (Figure 4.1). The salt solutions were poured slowly from the 4 L plastic jugs with the beaker tilted to make sure no air bubbles were being produced. Three vegetable oils were used because of their known impedances [172], inertness with the ultrasound scanners, and cost. The three oils were: Mazola corn oil (ACH Food Companies, Cordova, USA), Planters peanut oil (Kraft Canada Inc.,

Don Mills, Canada), and Aldo Petrelli olive oil (Imported by Anderson Watts Ltd., Vancouver, Canada). The values from literature places the corn oil's impedance as the highest at 1.41 MRayles, then olive oil at 1.32 MRayles, followed closely by peanut oil at 1.31 MRayles. One oil at a time (corn, olive, or peanut) was poured slowly on top of each salt solution concentration with the beaker tilted to reduce air entrapment. Only one oil of known impedance was needed to produce the data for the single calibration curve needed for a particular machine. Because there were several different types of oil to choose from, however, more than one oil was used. Therefore more than one calibration curve was determined for each ultrasound scanner. The interfaces for the Aloka SSD-900 were created in modified square plastic containers which allowed the cord of the Aloka's scanner head to protrude from the container without being bent. The filling procedure for the interfaces created for the Aloka SSD-900 was the same as for the Vevo 660.

TABLE 4.2

Aloka SD-900 with UST-588U-5 linear array scanner settings	
Frequency and Resolution:	7.5 MHz R-H
Acoustic Power Output (DVA):	100%
Display Depth (cm):	04
Gain:	70 (30 ~ 90)
Contrast:	1 (1 ~ 8)

If any air or salt solution bubbles were created, then a fine needle and syringe were used to eliminate the bubbles. A photographic gimballed pan-and-tilt head was modified to mount the scanner heads onto the photographic stage that was used (Figure 4.1). A photographic stage was used because it allowed the scanner head to be finely adjusted vertically with the help of a microscope's rack and pinion vertical adjustment. The rack and pinion allowed the interface to be viewed at exactly the focal point as indicated by an arrow on the output screen.

TABLE 4.3

FBG 32 image-grab software settings	
Brightness:	35
Contrast:	35
Field delay:	1
Line:	0
Align:	Any
Type:	None

The container with the oil-salt solution interface was re-positioned horizontally five times for the Vevo 660 and four times with the Aloka SSD-900 to make sure that a consistent measure of the interface was performed.   The difference in the number of interfaces imaged for the machines was necessitated by the differences in the shape of the containers used. The Vevo 660 interfaces were held in a circular beaker and the interface was first imaged in the middle, then pushed to the edge, imaged again and then rotated along the edge a further three equal increments until a full revolution of the beaker was imaged. The Aloka SSD-900 linear scanner was placed at the end of the square container and moved to 3 more positions along the container.

TABLE 4.4

Vevo 660 with VS-RMV30A scanner settings	
Frequency:	30 MHz
Attenuation:	0 dB
Gain:	4 dB
Frame rate:	16 Hz [15]
Field of view:	8 x 8 mm

After each salt solution and oil interface was scanned, the 900 mL beaker or the square plastic container was drained, washed with Sunlight dish soap, and then dried with a towel. Between each change in oil the scanning head was cleaned with Kimwipes

EX-L delicate task wipes. After the interfaces between the oil and salt solutions were imaged, they were saved either in a TIFF format (Vevo 660) or as a BMP format (Aloka SSD-900). Each interface from both machines was opened in Corel PHOTO-PAINT 10 (Corel Corporation, Ottawa, Canada). The interfaces were selected with a mask (photo editing software name for selected/analysed area on an image) and the histogram (distribution of pixel intensities) of the masked interface was used to find the maximum pixel value. On the histogram, the mouse cursor could be dragged to the maximum brightness level (between 0 and 255) to ascertain the maximum grey level intensity of the interface. Because the image output from the ultrasound machines was already a greyscale picture, the images were not converted to greyscale in PHOTO-PAINT and were therefore analyzed with the histogram as an RGB colour mode output (default) which gave the same result for the maximum pixel intensity. The ultrasound grey level intensities from the oil-salt solution interfaces for the Vevo 660 and Aloka SSD-900 can be found in Appendix C.
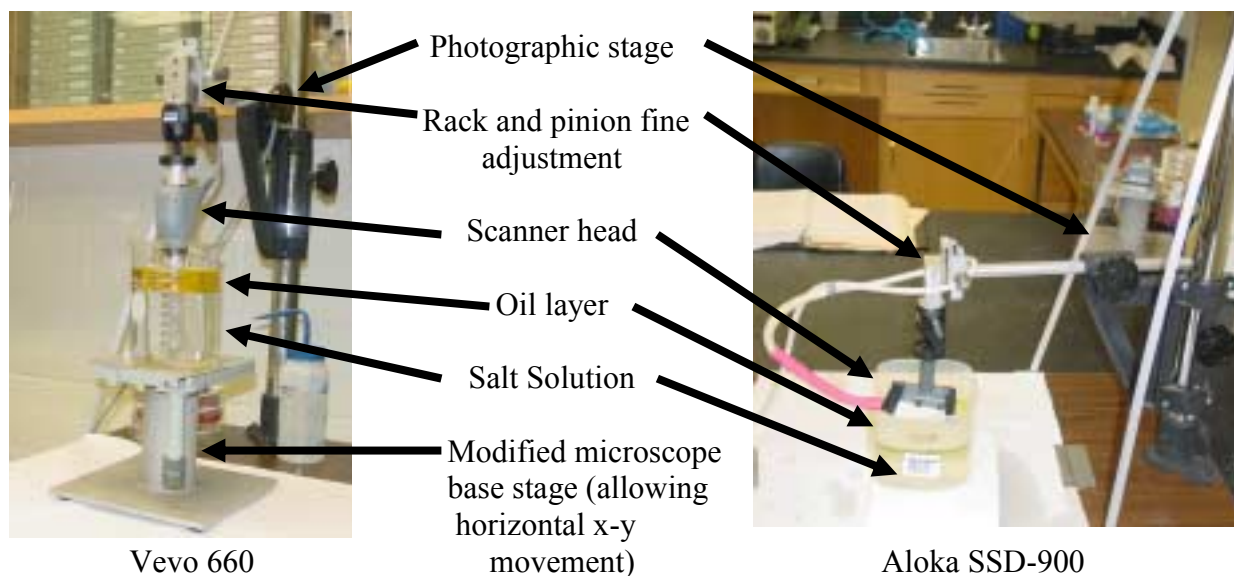
FIGURE 4.1   Vevo 660 and Aloka SSD-900 oil and salt solution interface setup.

4.2   Ultrasound Tissue Analysis

To test the calibration technique, tissue samples were sought that would have published impedance values. Porcine liver, kidney, and spleen tissue was selected having known published impedance values [173], [174]. The porcine tissue samples were imaged under corn oil to produce an interface that could be analysed.

The porcine tissue was received post-mortem from the University of Saskatchewan's Western College of Veterinary Medicine necropsy lab. The three tissues were removed from 10 high-health Landrace breed (4 to 7 week old) animals. The animals were involved in another study and therefore some of the tissues had been cut lengthwise to expose their interior structure. However, it is irrelevant to this experiment whether or not the tissue was cut because only the exterior tissue was of interest. The tissues were placed in plastic bags from the necropsy lab and left to sit at room temperature until the tissues could be imaged under the corn oil. For each sample of tissue, the tissue was removed from the plastic bag, washed with distilled water, dried with a paper towel, and digitally photographed with a 30 cm (12 inch) ruler as reference. The capsule surrounding the kidneys was removed by scoring the capsule with a scalpel and then pulling until it was separated from the kidney.   Appendix B contains photographs of the tissue used in the experiment.

After the photographs were taken, all three tissues (liver, kidney, and spleen) from the same animal were placed in a 20 x 14 x 7 cm glass pyrex dish. The glass dish with the tissue was filled with corn oil to a level that allowed the focal point of the ultrasound machines to be placed at the interface between the oil and tissue. If the tissue was tilted in the ultrasound image, the midpoint of the interfaces was adjusted to the focal point. Depending on the size of the tissue sample and the ultrasound machine, the interface was imaged anywhere between 4 to 8 times by moving the scanner head and the glass dish to different positions per tissue type from the 10 animals. The interfaces were analyzed the same manner as the oil – salt solution interfaces. Grey level results from the tissue experiment can be seen in Appendix D. Subsequent tissues were placed under the same oil in the same container.

4.3   Impedance, Error, and Statistical Analysis

Because the output of the ultrasound machines is a grey level intensity, an inverse mathematical process to calculate tissue impedance is necessary through the calibration curves (these curves will be shown and discussed in Chapter 5). From Excel's least squares fit, the following third-order polynomials are produced for the Vevo 660 and Aloka SSD-900 grey level output and reflection coefficient intensity curves for corn oil only:

$$\text{Vevo 660: } GL = 2\times10^{7}\cdot I_{RC}{}^{3} - 915744\cdot I_{RC}{}^{2} + 14862\cdot I_{RC} + 112.7 \qquad (4.3)$$

and

$$\text{Aloka SSD-900: } GL = 9\times10^{6}\cdot I_{RC}{}^{3} - 451783\cdot I_{RC}{}^{2} + 7309.1\cdot I_{RC} + 69.065 \qquad (4.4)$$

where GL is the grey level output from the salt-solution interfaces and I_{RC} is the calculated reflection coefficient intensity (equation 3.43) from the oil and salt-solution interfaces. The coefficient of determination for equations (4.3) and (4.4) are 0.925 and 0.928 respectively. Using Maple 7 (Maplesoft, Waterloo, Canada), equations (4.3) and (4.4) were each inverted to give expressions for I_{RC} in terms of GL.   Although easily used for computations within Excel, these expressions are extremely lengthy in form. The Maple 7 Output page is given in Appendix E and the inverted expressions are Equations (E.1) and (E.2) for the Vevo 660 and Aloka SSD-900 outputs respectively. The expression for tissue impedance (z_2) in terms of reflection coefficient intensity (I_{RC}) was obtained by inverting equation (4.5) to give equation (4.6) such that

$$I_{RC} = \left(\frac{z_2 - z_1}{z_2 + z_1}\right)^{2} \qquad (4.5)$$

and after inverting,

$$z_2 = \left[\frac{1 + \sqrt{I_{RC}}}{1 - \sqrt{I_{RC}}} \right] z_1 . \tag{4.6}$$

In order to make sure that the sampled tissue data were repeatable and were a proper measure of the tissue properties, statistical analysis was performed with both Microsoft Excel 2003 Data Analysis ToolPak and SPSS 12.0 (SPSS Ltd., Chicago, USA). Using SPSS, a two-tailed Pearson correlation analysis was performed on the oil and salt-solution data to confirm a relationship between the grey level output and the reflection coefficient for both machines and all three oils (corn, peanut, and olive). The significance of the Pearson correlation was set at $\alpha = 0.01$.

Excel's Data Analysis ToolPak was used to perform a two-factor with replication ANOVA for the different oils and the changing salt solutions. Descriptive analysis for the grey level at each percent salt solution and oil was performed to find the mean, standard deviation and standard error. A Two-Sample Assuming Unequal Variances t-test ($\alpha = 0.05$) was used to compare the means between the impedance outputs from the different machines.

Uncertainty error analysis for the calculated tissue impedance was estimated using the standard error in the grey level from the salt solutions and oil. Beginning with the calibration curves, and approximating a small portion of the curve as linear,

$$dI_{RC} = \frac{dGL}{m} , \tag{4.7}$$

where dI_{RC} is the error in the reflection coefficient intensity, m is the slope of the calibration curve in the region of interest, and dGL is the error in the grey level. The reflection coefficient intensity is given again by equation (4.8),

$$I_{RC} = \left(\frac{z_2 - z_1}{z_2 + z_1} \right)^2 \tag{4.8}$$

where z_2 is the lower interface impedance (tissue) and z_1 is the upper interface impedance (oil). If we differentiate equation (4.8) with respect to an arbitrary parameter, t, it becomes

$$\frac{dI_{RC}}{dt} = 2\left(\frac{z_2 - z_1}{z_2 + z_1}\right) \cdot \frac{d}{dt}\left(\frac{z_2 - z_1}{z_2 + z_1}\right),$$

(4.9)

or, assuming z_1 to be a constant (i.e., without error),

$$\frac{dI_{RC}}{dt} = \frac{dz_2}{dt} \cdot 2\left(\frac{z_2 - z_1}{z_2 + z_1}\right)\left(\frac{2z_1}{[z_2 + z_1]^2}\right),$$

(4.10)

$$dI_{RC} = dz_2 \cdot 2\left(\frac{z_2 - z_1}{z_2 + z_1}\right)\left(\frac{2z_1}{[z_2 + z_1]^2}\right)$$

(4.11)

where dz_2 is the error in the estimated impedance. Combining equation (4.7) and equation (4.11) gives an estimate of the error in the calculated tissue impedance from the error in the grey level and the slope in the region of the calculated tissue impedance. The final error equation is:

$$dz_2 = \frac{(z_2 + z_1)^3}{4mz_1(z_2 - z_1)}dGL .$$

(4.12)

The results of the ultrasound calibration curves and ultrasound tissue analysis will be presented in Chapter 5.

5.   RESULTS AND DISCUSSION

5.1   Calibration Curves

The calibration curves were the result of the oil-salt solution interface and the grey level ultrasound output from imaging the interfaces described in Section 4.1. For each calibration curve, the properties of the floating oil layer did not change, however the lower salt solution layer was varied in concentration from 0% to 20% salt concentration producing varying reflection coefficients intensities [I_{RC}] (Equation 3.43).

The research that was performed in this thesis used pixel intensities from the ultrasound scanner's output; therefore a quantitative measure of the intensity distribution was needed. Current research techniques that employ the grey level output, such as echotexture (Section 2.1.2), primarily use the mean and standard deviation of the pixel intensity. However, in this thesis the maximum grey level was chosen as a measure due to the ease of attaining the value and because the value was less prone to error. By selecting the entire interface and measuring the maximum grey level the procedure is much simpler than selecting a particular set of pixels for the mean and standard deviation measure. From Figure 5.1 it is evident that the measure of maximum pixel intensity is as informative as the mean pixel intensity for calibration and measurement purposes. The curves in Figure 5.1 were produced from the interface of corn oil and 0%, 10%, 15%, and 20% salt solutions. The reason that the 0, 10, 15, and 20 percent salt solutions were chosen for this experiment was because these values were from published data. All other values of salt impedance were interpolated from these four values. In comparing the mean and maximum grey level curves, the maximum grey level curve is expectedly higher than the mean grey level curve. Second order polynomial trend lines using MS Excel were superimposed to show how close the shapes of the curves are. The trend line for the maximum grey level is $y = -262556 x^2 + 9205.9 x + 118.05$ ($R^2 = 0.8997$) while the trend line equation for the mean grey level is $y = -274629 x^2 + 9359.1 x + 97.184$ ($R^2 = 0.9071$). Therefore, because the maximum and mean grey levels from

the reflection coefficient intensity are equally effective measures, maximum grey levels were used throughout the experiment and thesis.
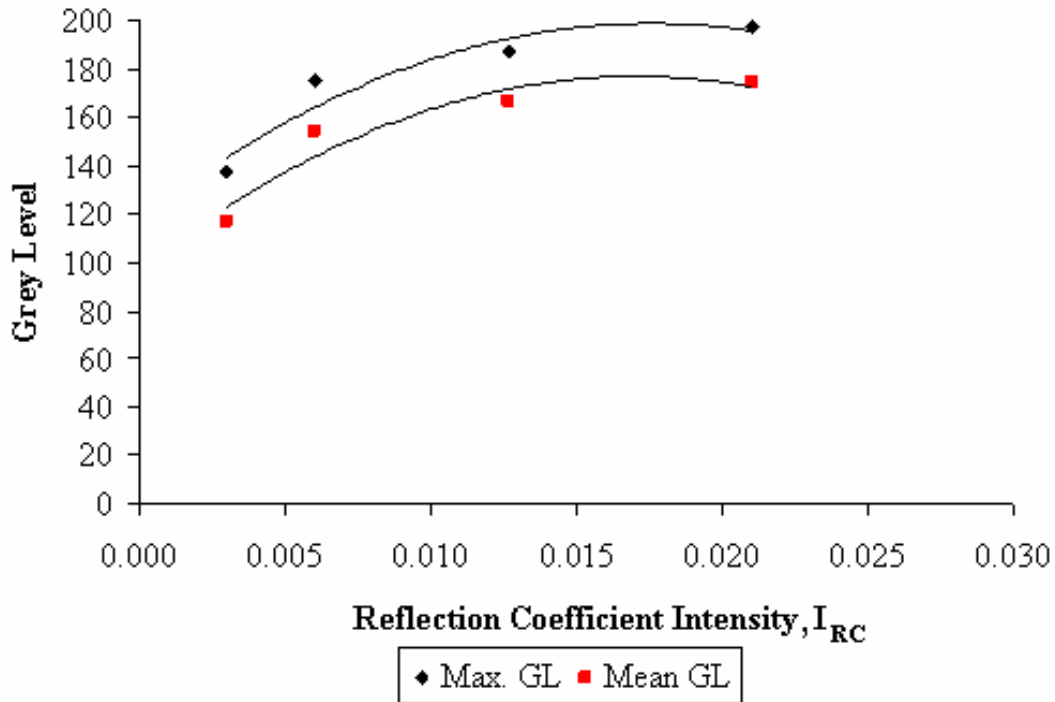
FIGURE 5.1   Comparison between the maximum and mean grey levels as a measure with the reflection coefficient intensity of corn oil.

The calibration curves for the Vevo 660 and Aloka SSD-900 are shown in Figures 5.2 and 5.3 respectively. The calibration curves from both machines have two distinct regions: a curved region at low I_{RC} values and a linear portion past $I_{RC} = 0.005$. A hypothesis why this is occurring is because of the logarithmic amplification within the ultrasound scanner's electronic image processing. At low I_{RC} values, the return signal intensity is weak and needs to be amplified more than return signals that are strong. As the intensity of the reflection becomes greater ($I_{RC} > 0.005$) the amplification is reduced. The curves from each oil, when imaged with the Vevo 660, were much more separated than that of the Aloka SSD-990. The grey level intensity of the corn oil is more predominant with the Vevo 660 while the olive oil is the greatest with the Aloka SSD-900.
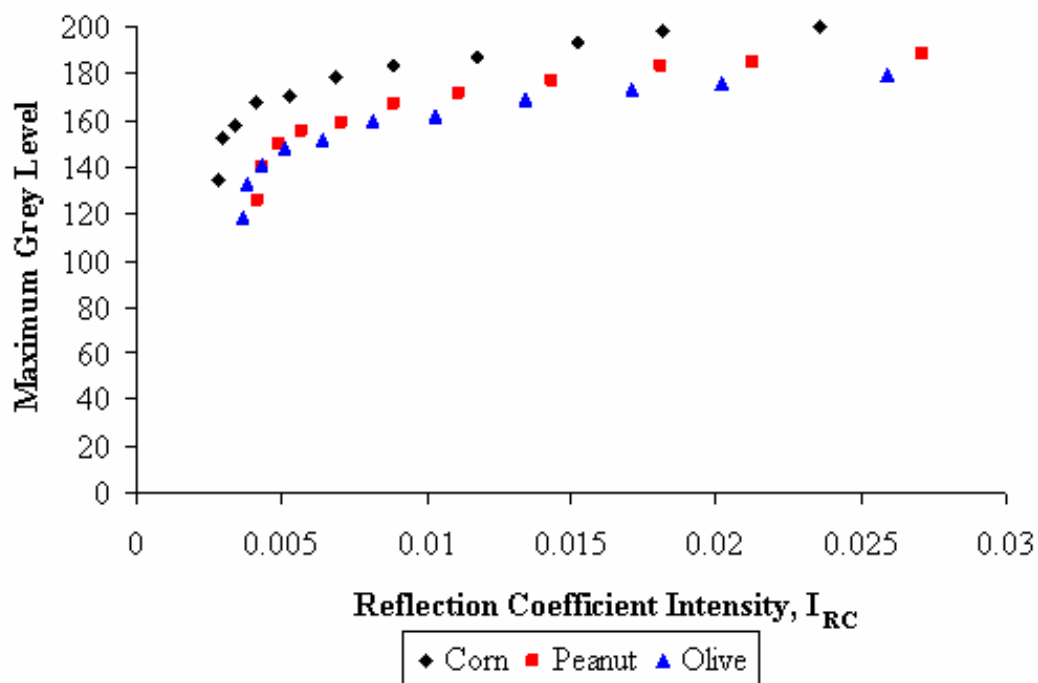
FIGURE 5.2   Vevo 660 calibration curves for corn, peanut and olive oil.
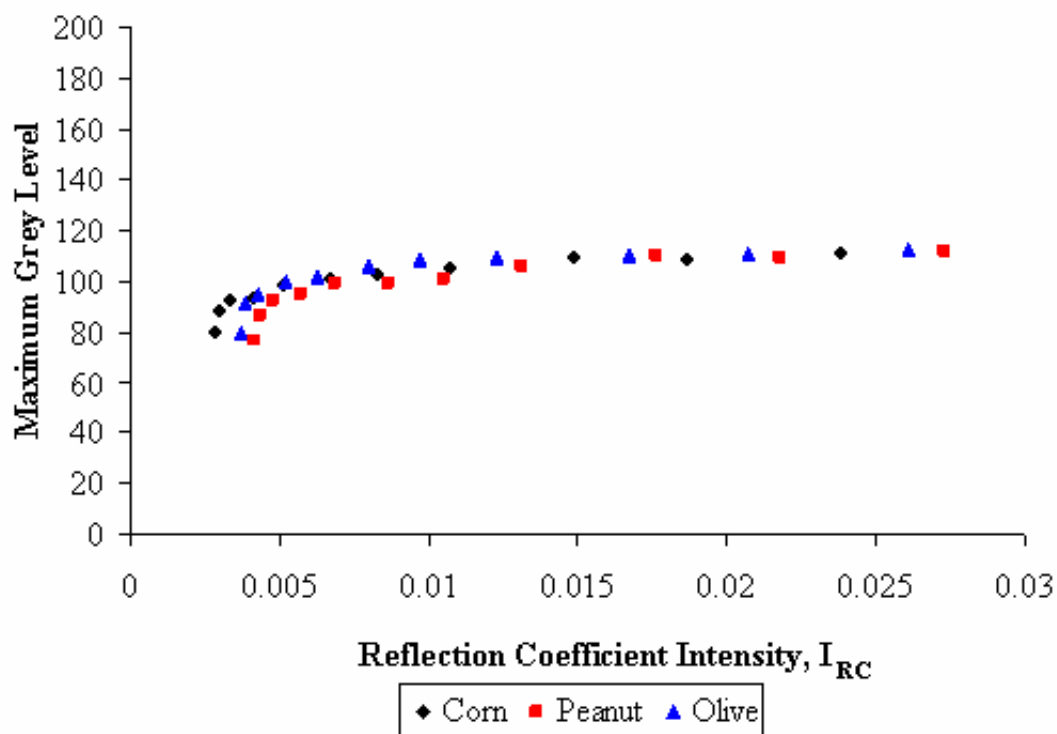
FIGURE 5.3   Aloka SSD-900 calibration curves for corn, peanut and olive oil.

The Vevo 660 operates at a much higher frequency (30 MHz) than the Aloka SSD-900
(7.5 MHz) and is likely much more sensitive to impedance changes due to its high
resolution. Slight variations in oil viscosities might cause huge variations in attenuation
or even velocity at high frequencies. The Vevo 660 grey level output was greater in
intensity and in range than the Aloka SSD-900 simply because the Vevo 660 employed
higher amplification and sensitivity. It is advantageous to have a large range for the
maximum grey level in view of the fact that there is a need to differentiate the tissues
from the grey level. MS Excel's ANOVA Two-Factor With Replication data analysis
was performed on the three oils and varying salt solution to show whether or not there is
any statistical interactions. The p-value results of the interaction analysis are
summarized in Table 5.1. It is obvious from Table 5.1 that there is no interaction
between the three oils and between the differing salt concentrations.

TABLE 5.1

Oil and salt solution interaction p-values		
	Oils	Salt solutions
Vevo 660	7.3×10^{-110}	1.5×10^{-153}
Aloka SSD-900	2.27×10^{-13}	9.89×10^{-67}

Pearson correlation analysis on the oil and salt concentrations was performed to confirm
a relationship between grey level output and the reflection coefficient intensity for both
machines and for all three oils. The results are summarized in Table 5.2. Because the p-
values are all greater than the cut-off of $\alpha = 0.05$, the results indicate a relationship
between the maximum grey level outputs and the reflection coefficient intensities. Note
that only one of the curves (corresponding to one of the oils or reference layers in
practice) is actually needed/used to calibrate for impedance.

TABLE 5.2

Pearson correlations: Grey level output and reflection coefficient intensity interaction

p-values

	Corn oil	Peanut oil	Olive oil
Vevo 660	0.869	0.879	0.876
Aloka SSD-900	0.849	0.839	0.756

5.2   Tissue Impedance Measurements

Once a calibration curve for a machine is produced, tissue impedance calculation is possible from the grey level output of an oil-tissue interface. By imaging tissue under a known impedance layer (oil) the grey level produced from the interface of the oil and tissue can be related back to the reflection coefficient intensity through an inverse mathematical process. The tissue's impedance can be solved through the reflection coefficient intensity equation (see Section 4.3). Liver, kidney, and spleen porcine tissues were imaged and impedance values calculated through the calibration curves. The impedance values with the calculated error (Equation 4.12) are summarized in table 5.3. The greatest acoustical impedance value for the examined tissue was kidney with liver then spleen following. The calculated percent difference between the machines is approximately 1%. This is important because with the method described within this thesis, it is possible to use any standard ultrasound scanner, after a calibration curve has been built, to experimentally derive tissue impedance values.

TABLE 5.3

	Liver	Kidney	Spleen
	Tissue impedance values [MRayles] (mean ± S.E.)		
Vevo 660	1.476 ± 0.020	1.486 ± 0.020	1.471 ± 0.020
Aloka SSD-900	1.467 ± 0.088	1.507 ± 0.088	1.457 ± 0.088
% Difference	0.61 %	1.39 %	0.96 %

Literature impedance values [173], [174] for porcine liver, kidney, and spleen are summarized in Table 5.4. The impedance values found in the literature are overlapping making tissue characterization difficult. The differences in impedance values with the method described in this thesis and the literature values may be because of temperature and frequency differences [10] and whether or not the tissues were taken *in vivo* and *in vitro* [175], [176].

TABLE 5.4

Literature values of impedance for porcine liver, kidney, and spleen [173, 174]	
	Impedance [MRayles]
Liver	1.567 – 1.62
Kidney	1.6 – 1.65
Spleen	1.6 – 1.619

The importance of using the calibration curves and solving for impedance is evident by referring to Table 5.5. Summarized in Table 5.5 are the maximum grey level values between the Vevo 660 and Aloka SSD-900. The average error between the two machines is 42%. Therefore the ability to characterize tissue using grey level intensities becomes questionable and research performed by different people using different machines is not verifiable.

TABLE 5.5

	Grey level intensity values (mean ± S.E.)		
	Liver	Kidney	Spleen
Vevo 660	140.5 ± 3.06	146.1 ± 2.80	131.5 ± 4.19
Aloka SSD-900	76.05 ± 2.08	87.28 ± 1.50	80.06 ± 1.20
% Difference	45.9 %	40.3 %	39.1 %

6. CONCLUSIONS AND RECOMMENDATIONS

6.1 Conclusions

In this thesis a calibration method is designed for use with any conventional ultrasound scanner. The method uses a calibration curve produced from a set of oil-salt solution interfaces. Each oil-solution interface is an interface of known impedances from which reflection coefficient intensity is calculated. Once the maximum grey level output and reflection coefficient intensity curve is built, any subsequent tissue analyzed with the ultrasound scanner will provide a maximum grey level with a corresponding impedance value (assuming the settings of the ultrasound scanner are still the same as the calibration curve settings and the impedance of the layer above the investigated tissue is known). Most current methods for characterizing tissue rely heavily on offline signal processing or specialized machines. As shown in this thesis, more direct approaches may be feasible.

The conclusion is that this thesis demonstrated that different ultrasound machines (differences such as image acquisition, frequency, and resolution) were able to produce acoustic impedance values that were comparable. Experimentally this is very useful because experiments derived from the approach in this thesis can be compared and verified from researcher to researcher.

Another conclusion is that using the maximum grey level intensity as opposed to the conventional mean grey level proved to be effective. The main difference between the two measures is that the maximum grey level curve will be greater than the mean grey level curve and that the determination of the maximum grey level from the ultrasound output is simpler.

6.2   Future Directions and Recommendations

This method of calibrating any conventional ultrasound scanner to acquire tissue impedance is a powerful tool and has far reaching applications and benefits. Although the current results allow a link to be established between grey level and tissue impedance, more elaborate studies need to be performed on tissues so the method can become more robust and accepted. Depending on the application of this method, whether it is human or veterinary medicine, extensive tissue studies are needed for normal tissue impedance so any deviation from the norm can be evaluated. This method can be incorporated in newly produced ultrasound scanners by allowing the manufacturer to calibrate the ultrasound scanner and then provide the settings to the end user which will allow tissue impedance assessment.

The conventional mathematical ultrasound model herein is primarily a reflection model which does not account for scatterers. The precise conditions under which the reflection model is sufficiently accurate must be established. In order to analyze quantitative ultrasound data for non-planar interior surfaces, the conventional mathematical model must be improved. A robust solution to the ultrasound model must be found that incorporates reflection, attenuation, and scattering.

Furthermore, perhaps this method of using the grey level output to assess tissue properties can be combined with the echotexture technique to establish a better link with tissue physiology.

REFERENCES

1. Harvey CJ, Pilcher JM, Eckersley RJ, Blomley MJ, Cosgrove DO. Advances in Ultrasound. Clinical Radiology 2002; 57: 157-177.

2. Zagzebski JA. Essentials of Ultrasound Physics. St. Louise: Mosby Inc.; 1996.

3. Kremkau FW. Diagnostic Ultrasound: Principles and Instruments. Philadelphia: W.B. Saunders Company; 2002.

4. Brant WE. Ultrasound. Philadelphia: Lippincott Williams & Wilkins; 2001.

5. Ginther OJ. Ultrasound Imaging and Animal Reproduction: Fundamentals. Cross Plains: Equiservices Publishing; 1995.

6. Brant WE. The Core Curriculum: Ultrasound. Philadelphia: Lippincott Williams & Wilkins; 2001.

7. Bronzino JD. The Biomedical Engineering Handbook. Boca Raton: CRC Press; 1995.

8. Heller M, Dietrich J. Ultrasound in Emergency Medicine. Philadelphia: W.B. Saunders Company; 1995.

9. Laugier P, Berger G, Perrin J. Scattering of ultrasound in biological tissues. ACTA Electronica 1984; 26: 81-93.

10. Jones JP. Ultrasonic Tissue Characterization: A review. ACTA Electronica 1984; 26: 3-31.

11. Taylor KJ, Wells PN. Tissue Characterization. Ultraosund in Medicine and Biology 1989; 15: 421-428.

12. Robinson DE, Wilson LS, Kossoff G. Shadowing and enhancement in ultrasonic echograms by reflection and refraction. Journal of Clinical Ultrasound 1981; 9: 181-188.

13. Richman TS, Taylor KJ, Kremkau FW. Propagation speed artifact in fatty tumor (myelolipoma). Journal of Ultrasound in Medicine 1983; 2: 45-47.

14. Wells PN. Ultrasound Imaging. Journal of Biomedical Engineering 1988; 10: 548-545.

15. Pierson RA, Ginther OJ. Ultrasonic evaluation of the corpu luteum of the mare. Theriogenology 1988; 29: 21-37.

16. Townsend DH, Ginther OJ. Size and shape changes in the preovulatory follicle in mares based on digital analysis of ultrasound images. Animal Reproductive Science 1989; 21: 63-71.

17. Townsend DH, Ginther OJ. Ultrasonic echogenity of developing corpera lutea in ponymares. Animal Reproductive Science 1989; 20: 143-153.

18. Griffin PG, Ginther OJ. Research applications of ultrasonic imaging in reproductive biology. Journal of Animal Science 1991; 70: 953-972.

19. Bergfelt DR, Ginther OJ. Ovarian, uterian, and embryo dynamics in horses versus ponies. Journal of Equine Veterinary Science 1996; 16: 66-72.

20. Tom, J. W., Pierson, R. A., and Adams, G. P. Ultrasound image attributes of bovine ovarian follicles assessed by computer-assited image analysis. Proceedings of the Annual Conference of the Canadian Society of Animal Science , 321. 1994.

21. Adams, G. P. and Pierson, R. A. Bovine model for the study of follicular dynamics in humans. Theriogenology 43, 113-120. 1995.

22. Pierson, R. A. and Adams, G. P. Computer-assisted image analusis, dignostic ultrasonography and ovulation induction: Strange bedfellows. Theriogenology 43, 105-112. 1995.

23. Singh J, Pierson RA, Adams GP. Ultrasound Image Attributes of the Bovine Corpus Luteum: Structural and Functional Correlates. Journal of Reproduction and Fertility 1997; 109: 35-44.

24. Singh J, Pierson RA, Adams GP. Ultrasound Image Attributes of Bovine Ovarian Follicles and Endocrine and Functional Correlates. Journal of Reproduction and Fertility 1998; 112: 19-29.

25. Beekman R, Visser LH. High-resolution sonography of the peripheral nervous system-a review of the litterature. European Journal of Neurology 2004; 11: 305-314.

26. Harland CC, Kale SG, Jackson P, Mortimer PS, Bamber JC. Differentiation of common benign pigmented skin lesions from melanoma by high-resolution ultrasound. British Journal of Dermatology 2000; 143: 289.

27. Momenan R, Wagner RF, Loew M, Insana MF, Garra BS. Characterization of Tissue from Ultrasound Images. IEEE Control Systems Magazine 1988; 8: 49-53.

28. Momenan, R., Wagner, R. F., Loew, M., Insana, M. F., and Garra, B. S. Unsupervised learning for characterization of tissue from acoustical speckle in ultrasound images. 935-940. 1987. Alexandria, VA, IEEE. Proceedings of the 1987 IEEE International Conference on Systems, Man and Cybernetics.

29. Lerski RA, Smith MJ, Morley P, Barnett E, Mills PR, Watkinson G, MacSween RNM. Discriminant analysis of ultrasonic texture data in diffuse alcoholic liver disease : 1. Fatty liver and cirrhosis. Ultrasonic Imaging 1981; 3: 164-172.

30. Ishimaru A, Kuga Y. Recent advances in multiple scattering theories and applications. IEICE Transactions on Electronics 1996; E79-C: 1295-1299.

31. Newhouse VL, Amir I. Estimation of scatterer volume density near a concentration gradient. Ultrasonic Imaging 1985; 7: 161-171.

32. Hosokawa T, Sigel B, Machi J, Kitamura H, Kolecki RV, Justin J, Feleppa EJ, Tuszynski G, Kakegawa T. Experimental assessment of spectrum analysis of

ultrasonic echoes as a method for estimating scatterer properties. Ultrasound in Medicine & Biology 1994; 20: 463-470.

33. Sigelmann RA, Reid JM. Analysis and measurement of ultrasound backscattering from an ensemble of scatterers excited by sine-wave bursts. Journal of the Acoustic Society of America 1973; 53: 1351-1359.

34. Wagner RF, Brown DG, Wear KA, Insana MF, Hall TJ. Statistical properties of the scatterer number density estimator. Ultrasonic Imaging 1991; 13: 192.

35. Waag RC. A review of tissue characterization from ultrasonic scattering. IEEE Transactions on Biomedical Engineering 1984; BME-31: 884-893.

36. Campbell JA, Waag RC. Normalisation of ultrasonic scattering measurements to obtain average differential scattering cross sections for tissue. Journal of the Acoustic Society of America 1983; 74: 393-399.

37. Leeman S, Jones JP. Tissue information from ultrasound scattering. Acoustic Imaging 1984; 13: 233-245.

38. Leeman S, Hutchins L, Heckmatt JZ, Jones JP. Characterization of human muscle. Journal of Ultrasound in Medicine 1983; 2: 159.

39. Lizzi FL, Greenbaum M, Feleppa EJ, Elbaum M, Coleman DJ. Theoretical framework for spectrum analysis in ultrasonic tissue characterization. Journal of the Acoustic Society of America 1983; 73: 1366-1373.

40. King DL, Lizzi FL, Feleppa EJ, Wai P, Yaremko MM. Focal and diffuse liver disease studied by quantitative micro-structural sonography. Radiology 1985; 155: 457-462.

41. Hill, C. R. Frequency and angular dependence of ultrasonic scattering from tissue. Linzer, M. 453, 28-30. 1975. NBS Special Publication. Ultrasonic tissue characterization.

42. Kimitsuki H, Parsons RE, Sigel B, Feleppa EJ, Golub RM, Justin J, Machi J, Rorke M, Sokil-Melgar J, Kodama I, Kurohiji T, Kakegawa T, Zaren HA. Effect of perfusion and blood content of ultrasonic backscattering of liver tissue. Ultraosund in Medicine and Biology 1993; 19: 39-43.

43. Bamber JD, Hill CR. Acoustic properties of normal and cancerous human liver: Dependance on pathologicla condition. Ultrasound in Medicine & Biology 1981; 7: 121-133.

44. Fellingham LL, Sommer FG. Ultrasonic characterization of tissue structures in the *in vivo* human liver and spleen. IEEE Transactions on Sonics and Ultrasonics 1984; SU31: 418-428.

45. Insana MF, Wagner RF, Brown DG, Hall TJ. Describing small-scale structure in random media using pulse-echo ultrasound. Journal of the Acoustic Society of America 1990; 8: 179-192.

46. Waag RC, Dalecki D, Christopher PE. Spectral power determinations of compressibility and density variations in model media and calf liver using ultrasound. Journal of the Acoustic Society of America 1988; 85: 431.

47. Zagzebski JA, Yao LX, Pozniak MA. Ultrasonic backscatter coefficient and its frequency dependence in normal liver. Journal of Ultrasound in Medicine 1991; 10: s22.

48. Mountford RA, Wells PN. Ultrasonic liver scanning: the quantitative analysis of the normal A-scan. Physics in Medicine and Biology 1972; 17: 14-25.

49. O'Donnell M, Miller JG. Quantitative broadband ultrasonic backscatter: An approach to nondestructive evaluation in acoustically inhomogeneous materials. Journal of Applied Physiology 1981; 52: 1056-1065.

50. Edee MKA. Tissue structure study through ultrasonic forward scattering. Ultrasonics 2000; 37: 645-656.

51. Berkoff AP, Van den Berg PM, Thijssen JM. Iterative calculation of reflective and transmitted acoustic waves at a rough interface. IEEE Transactions on ultrasonics, ferroelectrics, and frequency control 1995; 42: 663-671.

52. Sung-Rung H, Robert ML, Kevin JP. On estimating the amplitude of harmonic vibration from the Doppler spectrum of reflected signals. The Journal of the Acoustical Society of America 1990; 88: 2702-2712.

53. Sung-Rung H, Robert ML, Kevin JP. Time domain Doppler estimators of the amplitude of vibrating targets. The Journal of the Acoustical Society of America 1992; 91: 965-974.

54. Wells PN, Halliwell M, Skidmore R, Webb AJ, Woodcock JP. Tumour detection by ultrasonic Doppler blood flow signals. Ultrasonics 1977; 15: 231-232.

55. Jellins, J. B-mode and Doppler assessment of breast tissue. Jellins, J., Kossoff, G., and Croll, J. 215-220. 1985. Sidney, Proceedings of the Fourth International Congress on the Ultrasonics Examination of the Breast. Proceedings of the Fourth International Congress on the Ultrasonics Examination of the Breast.

56. Schoenberger SG, Sutherland CM, Robinsion AF. Breast Neoplasms: duplex sonographic imaging as a adjunct in diagnosis. Radiology 1988; 168: 665.

57. Scoutt L, Ramos I, Taylor KJ, Feyock A, Thompson S, Richter JO, Kornguth PJ, Snower D, Carter DC. Doppler examinations of breast masses. Radiology 1988; 21.

58. Ramos I, Taylor KJ, Kier R, Burns PN, Snower D, Carter DC. Tumor vascular signals in remal masses: detection with doppler US. Radiology 1988; 168: 633-637.

59. Miszalok V, Fritzsch T, Scherlt L. Myocardial perfusion defects in contrast echocardiology: spatial and temporal localisation. Ultrasound in Medicine & Biology 1986; 12: 379-383.

60. Krouskop TA, Dougherty DR, Levinson SF. A pulsed Doppler ultrasounic system for making noninvasive measurements of the mechanical properties of soft tissue. Journal of Rehabilitation Research and Development 1987; 14: 1-8.

61. Bateman DN, Leeman S, Metrewell C, Willson K. A non-invasive technique for gastric motility measurement. British Journal of Radiology 1977; 50: 526-527.

62. Muir TG, Carstensen EL. Prediction of nonlinear acoustic effects at biomedical frequencies and intensities. Ultrasound in Medicine & Biology 1980; 6: 345-357.

63. Carstensen EL, Law WK, McKay ND, Muir TG. Demonstration of nonlinear acoustical effects at biomedical frequencies and intensities. Ultrasound in Medicine & Biology 1980; 6: 359-368.

64. Bjorno L. Characterization of biological media by means of their non-linearity. Ultrasonics 1986; 24: 254-259.

65. Ichida N, Sato T, Linzer M. Imaging the nonlinear ultrasound parameter of a medium. Ultrasonic Imaging 1983; 5: 295-299.

66. Ichida N, Sato T, Miwa H, Murakami K. Real time non-linear parameter tomography using impulsive pumping waves. IEEE Transactions on Sonics and Ultrasonics 1984; SU-31: 635.

67. Bjorno L. Characterization of biological media by means of their non-linearity. Ultrasonics 1986; 24: 254-259.

68. Fields S, Dunn F. Correlation of echographic visualization of tissue with biological composition and physiological state. Journal of the Acoustic Society of America 1973; 54: 809-812.

69. Gao L, Parker KJ, Lerner RM, Levinson SF. Imaging of the elastic properties of tissue--A review. Ultrasound in Medicine & Biology 1996; 22: 959-977.

70. Parker KJ, Huang SR, Musulin RA, Lerner RM. Tissue response to mechanical vibrations for "sonoelasticity imaging". Ultrasound in Medicine & Biology 1990; 16: 241-246.

71. Oestreicher HL. Field and impedance of an oscillating sphere in a viscoelastic medium with an application to biophysics. Journal of the Acoustic Society of America 1951; 23: 707-714.

72. Von Gierke HE, Oestreicher HL, Franke EK, Parrack HO, Von Witten WW. Physics of vibrations in living tissue. Journal of Applied Physiology 1952; 4: 886-900.

73. Wilson LS, Robinson DE. Ultrasonic measurements of small displacements and deformations of tissue. Ultrasonic Imaging 1982; 4: 71-82.

74. Dickinson RJ, Hill CR. Measurement of soft tissue motion using correlation between A-scans. Ultrasound in Medicine & Biology 1982; 8: 263-271.

75. Tristam M, Barbosa DC, Cosgrove DO, Nassiri DK, Bamber JC, Hill CR. Ultrasonic study of in vivo kinetic characteristics of human tissues. Ultrasound in Medicine & Biology 1986; 12: 927-937.

76. Tristam M, Barbosa DC, Cosgrove DO, Bamber JC, Hill CR. Application of fourier analysis to clinical study of patterns of tissue movement. Ultrasound in Medicine & Biology 1988; 14: 695-707.

77. Birnholz JC, Farrell EE. Fetal lung development: compressibility as a measure of maturity. Radiology 1985; 157: 495-498.

78. Eisensher A, Schweg-Toffler E, Pelletier G, Jacquemard G. La palpation echographique rythmee-echosismographie. Journal De Radiologie 1983; 64: 255-261.

79. L.Gao, K. J. Parker R. M. Lerner and S. F. Levinson. Imaging of the elastic properties of tissue--a review. Ultrasound in Medicine & Biology 22[8], 959-977. 1996.

80. Lerner RM, Parker KJ, Holen J, Gramiak R, Waag RC. Sono-elasticity: Medical elasticity images derived from ultrasound signals in mechically vibrated targets. Acoustic Imaging 1988; 16: 317-327.

81. Lerner RM, Huang SR, Parker KJ. "Sonoelasticity" images derived from ultrasound signals in mechanically vibrated tissues. Ultrasound in Medicine & Biology 1990; 16: 231-239.

82. Lee F, Jr., Bronson JP, Lerner RM, Parker KJ, Huang SR, Roach DJ. Sonoelasticity imaging: results in in vitro tissue specimens. Radiology 1991; 181: 237-239.

83. Parker KJ, Lerner RM. Sonoelasticity of organs: Shear waves ring a bell. Journal of Ultrasound in Medicine 1992; 11: 387-392.

84. Rubens DJ, Hadley MA, Alam SK, Gao L, Mayer RD, Parker KJ. Sonoelasticity imaging of prostate cancer: in vitro results. Radiology 1995; 195: 379-383.

85. Ophir J, Cespedes I, Ponnekanti H, Yazdi Y, Li X. Elastography: A quantitative method for imaging the elasticity of biological tissues. Ultrasonic Imaging 1991; 13: 111-134.

86. O'Donnell M, Skovoroda AR, Shapo BM, Emelianov SY. Internal displacement and strain imaging using ultrasonic speckle tracking. IEEE Transactions on ultrasonics, ferroelectrics, and frequency control 1994; 41: 314-325.

87. Bertrand M, Meunier J, Doucet M, Ferland G. Ultrasonic biomechanical strain gauge based on speckle tracking. Proceeding of the IEEE Ultrasonics Symposium 1989; 2: 859-863.

88. Bohs LN, Trahey GE. A novel method for angle independent ultrasonic imaging of blood flow and tissue motion. IEEE Transactions on Biomedical Engineering 1991; BME-38: 280-286.

89. Haider MA, Holmes MH. Indentation of a thin compressible elastic layer: Approximate analytic and numerical solutions for rigid flat indenters. Journal of the Mechanics and Physics of Solids 1995; 43: 1199-1219.

90. Mak AL, Biphasic indentation of articular cartilage--I. Theoretical analysis. Journal of biomechanics 1987; 20: 703.

91. Mak AL, Biphasic indentation of articular cartilage--II. A numerical algorithm and. Journal of biomechanics 1989; 22: 853.

92. Han L, Noble JA, Burcher M. A novel ultrasound indentation system for measuring biomechanical properties of in vivo soft tissue. Ultrasound in Medicine & Biology 2003; 29: 813-823.

93. Chen EJ, Novakofski J, Jenking WK, O'Brian WJr. Young's modulus measurements of soft tissue with application to elasticity imaging. IEEE Transactions on ultrasonics, ferroelectrics, and frequency control 1996; 43: 191-194.

94. Ophir J, Kallel F, Varghese T, Konofagou E, Alam SKSK, Krouskop T, Garra B, Righetti R. Elastography. Comptes Rendus de l'Academie des Sciences - Series IV - Physics 2001; 2: 1193-1212.

95. Ophir J, Shawker TH, Mak AF, Miller JG, Flax S, Narayana PA, Jones JP. Attenuation estimation in reflection: Progress and prospects. Ultrasonic Imaging 1984; 6: 349-395.

96. Goss SA, Frizzell LA, Dunn F. Ultrasonic absorption and attenuation in mammalian tissues. Ultrasound in Medicine & Biology 1979; 5: 181-186.

97. Filipczynski L. Ultrasonic characterization of tissues in cardiology. Archives of Acoustics 1983; 8: 83-94.

98. Wells PNT. Absorption and dispersion of ultrasound in biological tissue. Ultrasound in Medicine & Biology 1975; 1: 396-376.

99. Cartensen EL, Schwan HP. Absorption of sound arising from the presence of intact cells in blood. Journal of the Acoustic Society of America 1959; 31: 185-189.

100. Pauly H, Schwan HP. Mechanism of absorption of ultrasound in liver tissue. Journal of the Acoustic Society of America 1971; 50: 692-699.

101. Dunn F, Edmonds PD, Fry WJ. Absorption and dispersion of ultrasound in biological media. In: Schwan HP, ed. Biological Engineering. New York: McGraw-Hill; 1969. pp 205-332.

102. Taboury J, Porcel A, Tubiana JM, Monnier JP. Cavernous hemangiomas of the liver studied by ultrasound. Radiology 1983; 149: 781-785.

103. Gosink BB, Lemon SK, Scheible W, Leopold GR. Accuracy of ultrasonography in diagnosis of hepatocellular disease. American Journal of Roentgenology 1979; 133: 19-23.

104. Jones, J. P. and Behrens, M. In vivo measurements of frequency-dependent attenuation in normal liver, pancreas, and spleen. Ultrasonic Imaging 3, 205. 1981.

105. Taylor KJ, Riely CA, Hammers L, Flax S, Weltin G. Quantitative US attenuation in normal liver and in patients with diffuse liver desease: importance of fat. Radiology 1986; 160: 65-71.

106.	Avtar SA. Ultrasonic attenuation in soft tissues: reasons for large magnitude and linear frequency dependance. Ultrasonic Imaging 1980; 2: 391-396.

107.	Ahuja SA. Tissue as a Voigt body for propagation of ultrasound. Ultrasonic Imaging 1979; 1: 136-143.

108.	Calderon C, Vilkomerson D, Mezrick R, Etzold KF, Kingsley B, Haskin M. Differences in the attenuation of ultrasound by normal, benign, and malignant breast tissue. Journal of Clinical Ultrasound 1976; 4: 249-254.

109.	Miller JG, Yuhas DE, Mimbs JW, Dierker SB, Busse LJ, Laterra JJ, Weiss AN, Sobel BE. Ultrasonic Tissue Characterization: Correlation Between Biochemical and Ultrasonic Indices of Myocardial Injury. IEEE Ultrasonics Symposium, Proc 1976; 76-CH-1120-5SU: 33-43.

110.	Fink M, Hottier F, Cardoso JF. Ultrasonic signal processing for in vivo attenuation measurements: short time Fourier analysis. Ultrasonic Imaging 1983; 5: 117-135.

111.	Ferrari L, Jones JP. The propagation of Gaussian modulated pulses in dissipative and/or dispersive media such as tissue. Ultrasound in Medicine & Biology 1985; 11: 299-305.

112.	Hutchins L, Leeman S. Pulse and impulse response in human tissue. Acoustic Imaging 1982; 12: 459-467.

113.	Dines KA, Kak AC. Ultrasonic attenuation tomography of soft tissue. Ultrasonic Imaging 1979; 1: 16-33.

114. Shmulewitz A. Ultrasonic multifeature maps of liver based on an amplitude loss technique and a conventional B-scan. IEEE Transactions on Biomedical Engineering 1992; 39: 445-449.

115. Hamamoto K, Andreas B, Shiina T, Ito M. Basic Investigations on reflection mode ultrasonic attenuation tomography. Japanese Journal of Applied Physics 1995; 34: 2812-2816.

116. Wild JJ, Reid JM. Further pilot echographic studies on the histological structures of tumors of the living intact human breast. American Journal of Pathology 1952; 28: 839.

117. Kossoff G, Fry EK, Jellins J. Average velocity of ultrasound in the human female breast. Journal of the Acoustic Society of America 1973; 54: 1730-1736.

118. Forsberg F, Conant EF, Russel KM, Moore JHJr. Quantitative Ultrasound Diagnosis of Silicon Breast Implants Rupture: An In Vitro Feasibility Study. Ultrasound in Medicine and Biology 1996; 22: 53-60.

119. Bamber JC, Hill CR, King JA. Acoustic properties of normal and cancerous human liver: Dependence on pathological condition. Ultrasound in Medicine & Biology 1981; 7: 121-133.

120. Cloostermans MJ, Mol H, Verhoef WA, Thijssen JM, Kubat K. In vitro estimation of acoustic parameters of the liver and correlations with pathology. Ultrasound in Medicine & Biology 1986; 12: 39-61.

121. El Fallah AI, Plantec MB, Ferrara KW. Ultrasonic measurement of breast tissue motion and the implications for velocity estimation. Ultrasound in Medicine & Biology 1997; 23: 1047-1057.

122. Glover GH. Computerized time-of-flight ultrasound tomography for breast examination. Ultrasound in Medicine & Biology 1977; 3: 1141.

123. Pedersen JF. SPMO 8613 A simple method for relative assessment of sound propagation velocity in breast tumors. Ultrasound in Medicine & Biology 1997; 23: S150.

124. Robinson DE, Chen F, Wilson LS. Measurement of velocity of propagation from ultrasonic pulse-echo data. Ultrasound in Medicine & Biology 1982; 8: 413-420.

125. Robinson DE, Chan F, Wilson LS. Measurement of velocity of propagation from ultrasonic pulse echo data. Ultrasound in Medicine & Biology 1982; 8: 321-332.

126.   measurement of sound velocity in liver by pulse-echo techniques : L. S. Wilson, C. F. Chen and D. E. Robinson, Ultrasonics Institute, 5 Hickson Road, Millers Point, NSW 2000, Australia. Ultrasonic Imaging 1983; 5: 168.

127. Ohtsuki, S., Soetanto, K., and Okujima, M. A technique with reference points image for in vivo measurements of sound velocity. Gill, S. R. and Dadd, M. J. 521. 1985. Elmsford, New York, Pergamon Press. Proceedings of the 4th Federation of Ultrasound in Medicine and Biology.

128. Bamber, J. C. and Abbott, C. The feasibility of measuring average sound speed in tissues using a real time scanner. Gill, S. R. and Dadd, M. J. 517. 1985. Elmsford, New York, Pergamon Press. WFUMB '85.

129. Robinson DE, Ophir J, Wilson LS, Chen CF. Pulse-Echo Ultrasound Speed Measurements: Progress and Prospects. Ultrasound in Medicine and Biology 1991; 17: 633-646.

130. A crossed beam method for ultrasonic speed measurement in tissue : D. J. Haumschild and J. F. Greenleaf, Department of Physiology and Biophysics, Biodynamics Research Unit, Mayo Clinic, Rochester, MN 55905. Ultrasonic Imaging 1983; 5: 168.

131. Kondo M, Takamizawa K, Hirama M, Okazaki K, Iinuma K, Takehara Y. An evaluation of an in vivo local sound speed estimation technique by the crossed beam method. Ultrasound in Medicine & Biology 1990; 16: 65-72.

132. Ophir J. Estimation of the speed of ultrasound propagation in biological tissues. A beam tracking method. IEEE Transactions on ultrasonics, ferroelectrics, and frequency control 1986; UFFC-33: 359-368.

133. Cespedes I, Ophir J, Huang Y. On the feasibility of pulse-echo speed of sound estimation in small regions: Simulation studies. Ultrasound in Medicine & Biology 1992; 18: 283-291.

134. Glover GH, Sharp JC. Reconstruction of ultrasound propagation speed distributions in soft tissue: time of flight tomography. IEEE Transactions on Sonics and Ultrasonics 1977; SU-24: 229-234.

135. Greenleaf JF, Johnson SA, Lent AH. Measurement of spatial distribution of refractive index in tissues by ultrasonic computer assissted tomography. Ultrasound in Medicine & Biology 1978; 3: 327-339.

136. Greenleaf JF, Johnson SA, Samayoam F, Duck FA. Algrebraic reconstruction of spatial distribution of acoustic velocity in tissue from their time of flight profiles. Acoustical Holography 1974; 6: 71-90.

137. Anderson AH. A ray tracing approach to restoration and resolution enhancement in experimental ultrasound tomography. Ultrasonic Imaging 1990; 12: 268-291.

138. Yiming, Tang. Approaches for measuring the properties of tissue with ultrasound. 1997. University of Saskatchewan.

139. Dolovich, A., Tang, Y., and Adams, G. An approach for measuring tissue properties with ultrasound. 56-57. 1998. Edmonton, Alberta. The Canadian Medical and Biological Engineering Society. 28-6-0098.

140. Siegal, M. and Ault, T. In situ calibration for quantitative ultrasonic imaging. Instrumentation & Measurement Magazine, IEEE 1[4], 9-18. 9-1-1998.

141. Siegel, M. Measurement issues in quantitative ultrasonic imaging. 1977. Ottawa, Ontario. IEEE Instrumentation and Measurement Technology Conference. 19-5-0077.

142. Dubovikova EA. Regularization, experimental errors, and accuracy estimation in tomography and interferometry. Journal Of The Optical Society Of America 1987; 4: 2033-2038.

143. Khuri-Yakub BT. Scanning acoustic microscopy. Ultrasonics 1992; 31: 361-372.

144. Hozumi N, Yamashita R, Lee C-K, Nagao M, Kobayashi K, Saijo Y, Tanaka M, Tanaka N, Ohtsuki S. Time-frequency analysis for pulse driven ultrasonic microscopy for biological tissue characterization. Ultrasonics 2004; 42: 717-722.

145. Santosh K, Tobocman W, Haacke EM, Izen SH. In vivo biomicroscopy with ultrasound. Ultrasonics 1987; 25: 274-282.

146. Santosh K, Tobocman W, Haacke EM, Boada F. In vivo biomicroscopy with ultrasound 2. Ultrasonics 1990; 28: 40-49.

147. Rizzatto G, Chersevani R. Breast ultrasound and new technologies. European Journal of Radiology 1998; 27: S242-S249.

148. Rallan D, Harland CC. Ultrasound in dermatology - basic principles and applications. Clinical and Experimental Dermatology 2003; 28: 632-638.

149. Cammarota T, Pinto F, Magliaro A, Sarno A. Current uses of diagnostic high-frequency US in dermatology. European Journal of Radiology 1998; 27: S215-S223.

150. Foster FS, Pavlin CJ, Harasiewicz KA, Christopher DA, Turnbull DH. Advances in ultrasound biomicroscopy. Ultrasound in Medicine & Biology 2000; 26: 1-27.

151. Liang K, Bennett SD, Khuri-Yakub BT, Kino GS. Precise Phase Measurements with the acoustical microscope. IEEE Transactions on Sonics and Ultrasonics 1985; 32: 266-273.

152. Liang K, Kino GS, Khuri-Yakub BT. Material characterization by the inversion of the V(Z). IEEE Transactions on Sonics and Ultrasonics 1985; 32: 213-224.

153. Gore JC, Leeman S. Ultrasonic backscattering from human tissue: a realistic model. Physics in Medicine and Biology 1977; 317-326.

154. Herment A, Peronneau P, Vaysse M. A new method of obtaining an acoustic impedance profile for characterization of tissue structures. Ultrasound in Medicine & Biology 1979; 5: 321-331.

155. Ogura I, Kidokoro T, Iinuma K, Takehara Y, Tanaka K, Matsuda A. Measurement of acoustic impedance of skin. Ultrasound in Medicine 1978; 4: 535-543.

156. Tobocman W, Santosh K, Carter JR, Haacke EM. Tissue characterization of arteries with 4 MHz ultrasound. Ultrasonics 1995; 33: 331-339.

157. Jones JP, Cole-Beuglet C. In vivo characterization of several lesions in the eye using ultrasonic impediography. Acoustic Imaging 1980; 8: 539-546.

158. Jones JP, Wright HA. A new broad-band ultrasonic technique with biomedical implications. Journal of the Acoustic Society of America 1972; 52: 178.

159. Leeman S. Impediography equations. Acoustic Imaging 1980; 8: 517-525.

160. Goupillaud PL. An approach to inverse filtering of near-surface layer effects from seismic records. Geophysics 1961; 26: 754-760.

161. Pedersen PCLI. Ultrasound System for Acoustic Impedance Profile Reconstruction. IEEE Engineering in Medicine & Biology Society 10th Annual International Conference 1988; 1: 468-469.

162. Lifshitz, I. The reconstruction of the acoustical impedance profile of a multi-layered medium. 1988. Drexel University.

163. Bai, J. and Qi, W. Acoustic impedance reconstruction of layered media with high resolution. IEEE Engineering in Medicine & Biology Society 12, 283-284. 1990. Philadelphia, PA, IEEE Engineering in Medicine & Biology Society. Proceedings of the Twelfth Annual Internation Conference of the IEEE Engineering in Medicine & Biology Society. 1-11-1990.

164. M.Bramanti. A method for obtaining more information from attenuation based material testing techniques. IEEE Transactions on Instrumentation and Measurement 1989; 38: 130-132.

165. Bramanti M. Single Procedure to Measure Ultrasound Characteristic Wave Impedance, Attenuation, and Propogation Velocity in Materials. NDT&E International 1993; 26: 283-286.

166. Gunarathne GPP, Christidis K. Material characterization in situ using ultrasound measurements. Instrumentation and Measurement, IEEE Transactions on 2002; 51: 368-373.

167. Hull JB, Langton CM, Jones AR. Identification and characterization of materials by broadband ultrasonic attenuation analysis. Journal of Material Processing Technology 1996; 56: 148-157.

168. Bray DE, Roderic SK. Nondestructive evaluation: A tool for design, manufacturing, and service. New York, NY: McGraw-Hill Book Company; 1989.

169. Shutilov VA. Fundamental Physics of Ultrasound. New York: Gordon and Breach Science Publishers; 1988.

170. CRC Handbook of Chemistry and Physics. Boca Raton: CRC Press Inc.; 1982.

171. Standard Test Method for: Density, Relative Density (Specific Gravity), or API Gravity of Crude Petroleum and Liquid Petroleum Products by Hydrometer Method; Standard Designation: D1298-85. In: Storer RA, ed. 1987 Annual Book

of ASTM Standards: Petroleum Products, Lubricants, and Fossil Fuels. Philadelphia, PA: ASTM; 1987. pp 658-663.

172. Pederson, L. Acoustic Properties. Pederson, Laust. 2004. Sunnyvale, CA, Onda Corp. http://www.ondacorp.com/tecref_acoustictable.html.

173. Goss SA, Johnston RL, Dunn F. Comprehensive compilation of empirical ultrasound properties of mammalian tissues. Journal of the Acoustic Society of America 1978; 64: 423-457.

174. Goss SA, Johnston RL, Dunn F. Compilation of empirical ultrasound properties of mammalian tissues II. Journal of the Acoustic Society of America 1980; 68: 93-108.

175. O'Donnell M, Mimbs JW, Sobel BE, Miller JG. Ultrasonic attenuation of myocardial tissue: Dependence on time after excision and on temperature. The Journal of the Acoustical Society of America 1977; 62: 1054-1057.

176. Bamber JC, Fry MJ, Hill CR, Dunn F. Ultrasonic attenuation and backscattering by mammalian organs as a function of time after excision. Ultrasound in Medicine & Biology 1977; 3: 15-20.

APPENDIX A. Reproduced Hydrometer Correction Table

TABLE A.1   Hydrometer temperature correction table

Ever Ready Thermometer Co., Inc.
Correction for Specific Gravity Hydrometers 60F/60F (15.56C/15.56C)

Degrees F	68	77	86	95	104	113	122	131	140	149	158	167	176	185	194	203	212
Degrees C	20	25	30	35	40	45	50	55	60	65	70	75	80	85	90	95	100
0.700	0.5	1.2	1.9	2.6	3.3	4.0	4.7	5.4	6.1	6.8	7.5	8.2	8.9	9.6	10.3	11	11.7
0.800	0.6	1.4	2.2	3.0	3.9	4.6	5.4	6.2	7.0	7.8	8.6	9.4	10.2	11.0	11.8	12.6	13.4
0.900	0.6	1.6	2.6	3.6	4.6	5.6	6.6	7.6	8.6	9.6	10.6	11.6	12.6	13.6	14.6	15.6	16.6
1.000	0.7	1.8	2.9	4.0	5.1	6.2	7.3	8.4	9.5	10.6	11.7	12.8	13.9	15.0	16.1	17.2	18.1
1.100	0.8	1.9	3.0	4.1	5.2	6.3	7.4	8.5	9.6	10.7	11.8	12.9	14.0	15.1	16.1	17.1	18.3
1.200	0.8	2.0	3.2	4.4	5.6	6.8	8.0	9.2	10.4	11.6	12.8	14.0	15.2	16.4	17.6	18.8	20
1.300	0.9	2.3	3.7	5.1	6.5	7.9	9.3	10.7	12.1	13.5	14.9	16.3	17.7	19.1	20.5	21.9	23
1.400	1.0	2.5	4.0	5.5	7.0	8.5	10.0	11.5	13.0	14.5	16.0	17.5	19.0	20.5	22.0	23.5	25
1.500	1.1	2.6	4.1	5.6	7.1	8.6	10.1	11.6	13.1	14.6	16.1	17.6	19.1	20.6	22.1	23.6	25.1
1.600	1.1	2.8	4.5	6.2	7.9	9.6	11.3	13.0	14.7	16.4	18.1	19.8	21.5	23.2	24.9	26.6	28.3
1.700	1.2	3.2	5.2	7.2	9.2	11.2	13.2	15.2	17.2	19.2	21.2	23.2	25.2	27.2	29.2	31.2	33.2
1.800	1.3	3.3	5.3	7.3	9.3	11.3	13.3	15.3	17.3	19.3	21.3	23.3	25.3	27.3	29.3	31.3	33.3
1.900	1.4	3.4	5.5	7.6	9.7	11.8	13.9	16.0	18.1	20.2	22.3	24.4	26.5	30.7	30.7	32.8	35
2.000	1.4	3.5	5.6	7.7	9.8	11.9	14.0	16.1	18.2	20.3	22.4	24.5	26.7	30.8	31.7	32.9	39.9

SPECIFIC GRAVITY

Note: To use chart, choose specific gravity reading and temperature closest to the unknown sample
and apply correction by moving the decimal point [3] places to the left. For example the
correction factor specific gravity 1,000 at 77F (25C) would be +.0018. For corrections not on
chart, one must interpolate between given corrections.

APPENDIX B.   Photographs of the Tissues Used in the Experiment

Tissues (liver, kidney, and spleen) from 10 pigs (*Sus scrofa*) were collected and imaged under corn oil with ultrasound. Each of the animal's tissues was photographed prior to the ultrasound imaging. Figures B.1 to B.10 give the photographs of the tissues for the 10 animals.

Figure B.1   Liver, Kidney, Spleen
              Animal 1

Figure B.2   Liver, Kidney, Spleen
              Animal 2
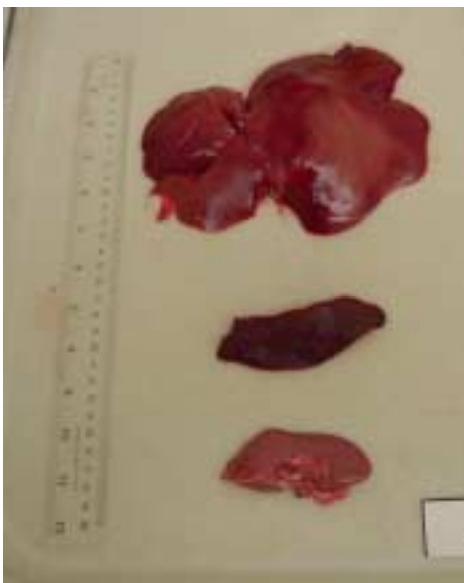
Figure B.3   Liver, Kidney, Spleen
              Animal 3

Figure B.4   Liver, Kidney, Spleen
              Animal 4

Figure B.5   Liver, Kidney, Spleen
Animal 5
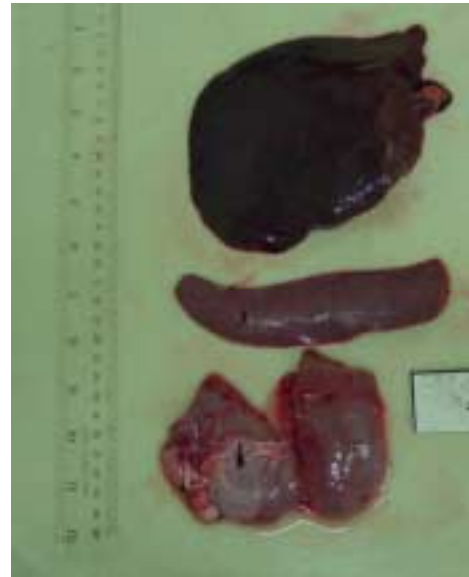
Figure B.6   Liver, Kidney, Spleen
Animal 6
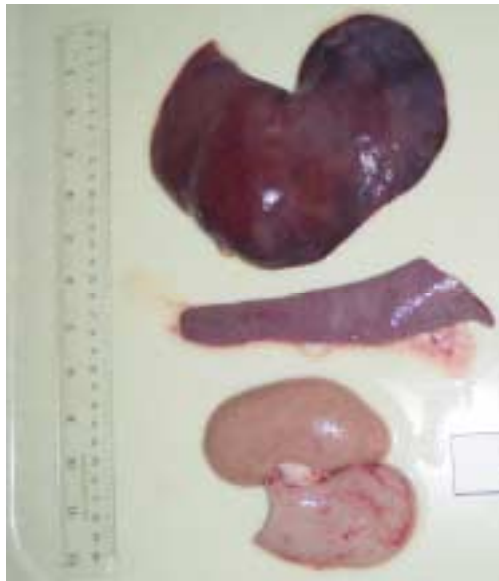
Figure B.7   Liver, Kidney, Spleen
Animal 7

Figure B.8   Liver, Kidney, Spleen
Animal 8
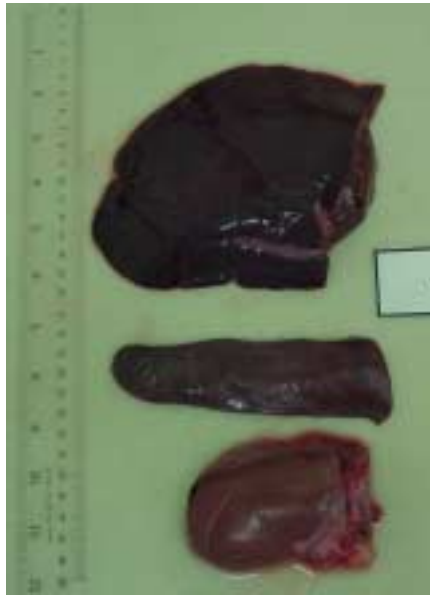
Figure B.9   Liver, Kidney, Spleen
Animal 9

Figure B.10   Liver, Kidney, Spleen
Animal 10

APPENDIX C. Ultrasound oil- salt solution data

Table C.1   Vevo 660 ultrasound grey level intensities for oil- salt solutions interfaces

Corn Oil										
0%	**2%**	**4%**	**6%**	**8%**	**10%**	**12%**	**14%**	**16%**	**18%**	**20%**
137	153	157	167	169	180	184	188	192	199	198
136	151	158	165	170	177	183	187	193	198	201
134	154	158	168	168	178	183	186	192	198	201
134	152	157	169	173	177	184	187	194	199	201
133	152	158	168	173	180	183	185	193	196	199

Grey Levels:

Peanut Oil										
0%	**2%**	**4%**	**6%**	**8%**	**10%**	**12%**	**14%**	**16%**	**18%**	**20%**
125	140	149	155	158	167	172	176	181	185	190
128	139	150	154	159	166	170	178	181	184	187
121	140	149	156	158	167	173	177	184	187	189
125	140	150	156	158	166	171	178	184	183	190
127	139	150	153	160	167	172	175	184	184	187

Grey Levels:

Olive Oil										
0%	**2%**	**4%**	**6%**	**8%**	**10%**	**12%**	**14%**	**16%**	**18%**	**20%**
117	134	141	146	153	159	159	166	171	175	179
120	132	140	150	151	159	163	169	174	176	181
121	133	142	148	151	159	163	169	173	176	181
117	133	142	147	153	159	161	169	174	174	178
117	133	141	147	152	160	162	168	174	177	180

Grey Levels:

Table C.2   Aloka SSD-900 ultrasound grey level intensities for oil- salt solutions
              interfaces

Corn oil										
0%	**2%**	**4%**	**6%**	**8%**	**10%**	**12%**	**14%**	**16%**	**18%**	**20%**
76	89	91	91	99	102	105	109	109	109	114
78	88	92	91	99	98	101	100	109	107	110
84	88	92	94	97	101	99	102	111	108	111
83	89	95	97	98	102	105	108	107	110	108

Peanut Oil										
0%	**2%**	**4%**	**6%**	**8%**	**10%**	**12%**	**14%**	**16%**	**18%**	**20%**
72	85	91	97	99	98	101	105	109	108	115
75	86	91	96	102	101	100	108	111	110	114
76	86	92	92	101	100	102	107	110	111	107
82	88	95	96	94	98	101	102	110	109	112

Olive Oil										
0%	**2%**	**4%**	**6%**	**8%**	**10%**	**12%**	**14%**	**16%**	**18%**	**20%**
78	92	97	100	101	106	109	110	111	111	112
78	91	97	100	101	106	108	109	109	111	112
80	91	92	100	101	105	109	109	110	111	112
83	94	95	101	103	107	108	110	111	111	114

Grey Levels:

APPENDIX D.   Ultrasound oil-tissue data

Table D.1   Vevo 660 ultrasound grey level intensities for oil-tissues interfaces

	Corn oil + Liver									
Animals:	1	2	3	4	5	6	7	8	9	10
Grey Levels:	159	158	139	164	61	160	160	112	164	140
	156	142	99	101	137	128	156	155	153	117
	157	149	94	104	171	159	139	144	138	130
	152	135	125	128	140	162	127	111	144	138
	148		112		164	125	161	141	146	149
	162		140				166		163	
	162								170	
	113									

	Corn oil + Kidney									
Animals:	1	2	3	4	5	6	7	8	9	10
Grey Levels:	184	133	119	161	139	142	143	162	133	161
	179	129	97	150	160	141	136	120	133	170
	183	133	119	159	165	158	128	133	158	174
	186	124	133	158	153	148	132	161	131	131
	182	114	154	134	149	123	115	124		165
	164		149			146				172
	163					122				

	Corn oil + Spleen									
Animals:	1	2	3	4	5	6	7	8	9	10
Grey Levels:	123	162	126	144	67	168	101	132	85	126
	159	153	135	171	112	171	131	158	110	140
	155	139	138	146	63	147	161	162	72	114
	168	125	116	135	78	138	153	162	126	111
		137	109	159	110	169	149	163	74	
		155			68				145	
					155				91	

Table D.2   Aloka SSD-900 ultrasound grey level intensities for oil-tissues interfaces

Corn oil + Liver									
1	**2**	**3**	**4**	**5**	**6**	**7**	**8**	**9**	**10**
66	87	60	40	76	64	91	78	101	107
73	84	63	41	103	80	77	74	105	89
64	78	71	55	80	83	76	70	98	97
78	74	60	52	56	73	83	70	86	87
77	94	63	42	68	77	66	63	78	84
86	86		53	71	87				90
									100

Animals: above columns 1–10. Grey Levels: data rows.

Corn oil + Kidney									
1	**2**	**3**	**4**	**5**	**6**	**7**	**8**	**9**	**10**
89	86	84	92	90	59	100	89	82	100
106	76	104	90	92	92	83	83	87	86
92	70	94	73	88	103	87	85	78	92
102	97	62	83	88	84	108	87	89	98
74	64	92	92	88	107	91	66	79	84
96	76	86						88	

Corn oil + Spleen									
1	**2**	**3**	**4**	**5**	**6**	**7**	**8**	**9**	**10**
87	85	75	83	85	87	77	92	77	64
74	86	76	92	86	86	91	92	72	64
70	76	66	68	88	76	88	86	80	54
86	84	83	87	87	70	72	91	76	84
73	80	80	88	73	77	92	80	72	83
									82

APPENDIX E. Expressions for reflection coefficient intensity in terms of grey level

Vevo 660 inversion equation from the third order polynomial (Equation E.1):

$$I_{RC} = 0.8 \times 10^{-6} \left(-0.9635 \times 10^{13} + 0.4883 \times 10^{11} \cdot GL + 31250 \cdot \sqrt{0.9507 \times 10^{15} - 0.9635 \times 10^{15} \cdot GL + 0.2441 \times 10^{13} \cdot GL^2} \right)^{1/3}$$

$$- \frac{18.4489}{\left(-0.9635 \times 10^{13} + 0.4883 \times 10^{11} \cdot GL + 31250 \cdot \sqrt{0.9507 \times 10^{17} - 0.9635 \times 10^{15} \cdot GL + 0.2441 \times 10^{13} \cdot GL^2} \right)^{1/3}} + 0.01526 .$$

Aloka SSD-900 inversion equation from the third order polynomial (Equation E.2):

$$I_{RC} = 0.3704 \times 10^{-7} \left(-0.1170 \times 10^{18} + 0.1094 \times 10^{16} \cdot GL + 0.1350 \times 10^{7} \sqrt{0.7517 \times 10^{22} - 0.1405 \times 10^{21} \cdot GL + 0.6561 \times 10^{18} \cdot GL^2} \right)^{1/3}$$

$$+ \frac{250.4511}{\left(-0.1170 \times 10^{18} + 0.1094 \times 10^{16} \cdot GL + 0.1350 \times 10^{7} \sqrt{0.7517 \times 10^{22} - 0.1405 \times 10^{21} \cdot GL + 0.6561 \times 10^{18} \cdot GL^2} \right)^{1/3}} + 0.01673 .$$